Doctoral Dissertation

Olfactory cortex ventral tenia tecta neurons encode the distinct context-dependent behavioral states of goal-directed behaviors

Kazuki Shiotani

Graduate School of Brain Science, Doshisha University

A thesis submitted for the degree of

Doctor of Philosophy in Science

Mar. 2021

Abstract

Sensory perception emerges from the integration of bottom-up and top-down inputs. The values of odorants do not consist of sensory information alone but are determined by top-down information. The olfactory cortex receives not only the afferent inputs from the olfactory bulb (OB) but also the efferent inputs from the higher brain regions. The ventral tenia tecta (vTT) is a component of the olfactory cortex and receives both bottom-up odor signals and top-down higher signals. However, the roles of the vTT in odor-coding and integration of inputs are poorly understood. Here, we investigated the involvement of the vTT in these processes by recording activity from individual vTT neurons during performance of two types of odor-guided reward-directed tasks, i.e., odor-guided go/no-go task with water reward and odor-guided eating/no-eating task with food reward, in mice. We report here that individual vTT cells were highly tuned to a specific behavioral epoch of the learned tasks, whereby the duration of increased firing correlated with the temporal length of the behavioral epoch across the distinct task. The peak times of increased firing in all recorded vTT cells encompassed almost the entire temporal window of both tasks. The firing patterns of vTT cells had contextual response changes despite the same behavioral state, indicating that individual vTT cell firing was tuned to a specific behavioral context and was thus dependent on specific task-elements during task progression rather than on specific behaviors. Moreover, we found that the vTT receives inputs from the medial prefrontal cortex (mPFC) and is interconnected with other olfactory cortical areas anatomically. Collectively, our results indicate that vTT cells are selectively activated during a specific behavioral context and that the function of the vTT changes

dynamically in a context-dependent manner during goal-directed behaviors. These results also suggest that the context-dependent firing patterns of the vTT cells are represented by the top-down inputs from the mPFC and vTT cells convey the context-dependent information to other olfactory cortical areas for adaptive odor-guided behaviors.

Acknowledgments

I would like to express my deepest gratitude to my supervisors, Dr. Hiroyuki Manabe and Dr. Yoshio Sakurai for their continuous guidance, scientific advice, and encouragement during the last 5 years. I'm grateful to Dr. Junya Hirokawa, Mr. Yuta Tanisumi, Dr. Koshi Murata, Dr. Kensaku Mori, and the past and present lab members for their encouragement and insightful comments on this research. Without them, this study would not have been possible. I would like to give special thanks to my thesis committee, Dr. Susumu Takahashi and Dr. Jun Motoyama for their time and efforts in my examination. I'm also grateful to the Japan Society for the Promotion of Science (JSPS) and Doshisha University for their financial support and Mr. Hideki Tanisumi for providing mouse illustrations in Figures. Finally, I wish to extend my sincere gratitude to my family for their understanding, support, and encouragement. I don't think I could have achieved this study without their dedication.

Parts of this doctoral dissertation has been already published.

Table of contents

List of figures and tables

Figures

Tables

Chapter 1. Introduction

1.1. Olfaction

Olfactory neuronal circuits translate odor cues into various behavioral responses that enable mammals to find and locate foods, mates, and predators. Almost all volatile chemicals (low-molecular-weight <300 Da) can be perceived as distinct from other molecules with nose (Herrmann, 2010). Although humans recognize fewer molecules than most of other mammals, we seem to be able to discriminate among ~10,000 different odors (Menini et al., 2004). How can we discriminate them? Odorants are initially detected by odorant receptors (ORs) on olfactory sensory neurons (OSNs) in the nasal olfactory epithelium (OE) (Buck and Axel, 1991) (Figure 1). Each OSNs expresses only one type of the OR genes (Malnic et al., 1999; Niimura and Nei, 2005). The number of functional ORs varies across species and has been estimated to be ~1,000 in rodents, ~ 300 in humans, and ~60-350 in insects (Go and Niimura 2008, Olender et al. 2013, Touhara and Vosshall 2009). An odorant molecule can be bound with multiple types of ORs. The important point is that the combination of ORs for detecting odor molecules is unique to each of the molecules and generates a specific pattern of signals to the brain. Axons of OSNs expressing a given one type of OR converge onto typically two discrete small spherical constitutions of common mirror-placed locations in the olfactory bulb (OB) called glomeruli (Uchida et al., 2014). Glomeruli are relatively large spherical neuropils, within which axons of OSNs form glutamatergic excitatory synaptic connections on dendrites of mitral and tufted cells (M/T cells), the output neurons of the OB (Mori

and Sakano, 2011). M cells respond to odorants in regular spiking, whereas T cells respond in bursting and tent to be more sensitive to odor stimuli (Cavarretta et al., 2018). Each glomerulus can be considered as an olfactory axon convergence center for inputs originating from one type of OR; the OR-specific signal is transmitted to M/T cells innervating the glomerulus, thereby forming a map of receptor identity. An individual glomerulus receives converging axonal inputs from several thousand OSNs (each expressing the same odorant receptor) and is innervated by primary dendrites of ~20 mitral cells (Royet et al., 1998). Within the OB, the odor information coded is processed in the local neuronal circuits. It's conveyed by M/T cells, whose axons pass through the lateral olfactory tract (LOT) to various areas of the olfactory cortex (OC) (Mori et al., 1999; Shepherd et al., 2004).

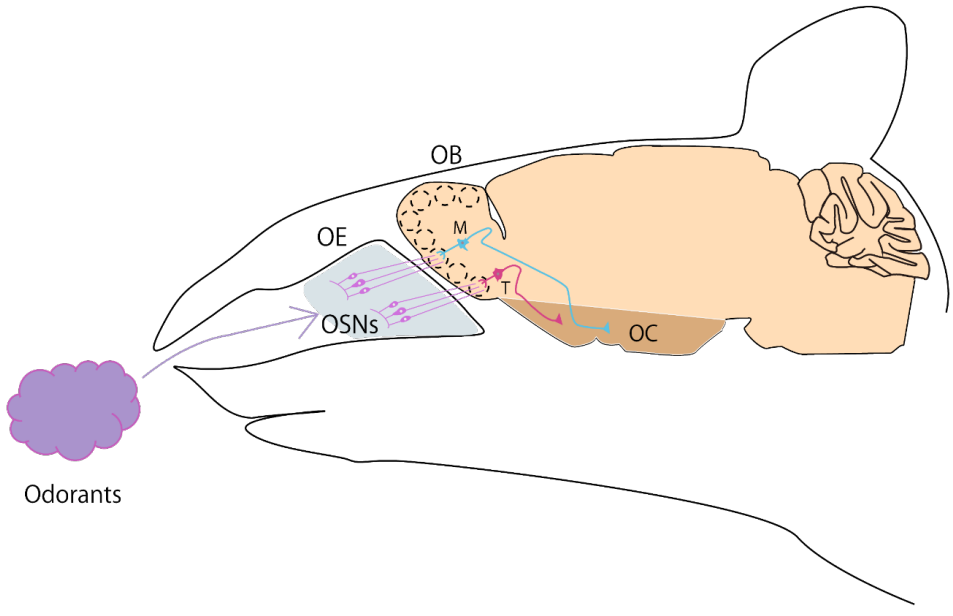

Figure 1 | Schematic illustration of the mouse olfactory system.

Informational flow for olfactory signal processing. In the OE, odorants are detected by OR molecules expressed in OSNs. Combined odorant signals are converted to a topographic map of activated glomeruli (dotted circle) in the OB. Odor information is conveyed by mitral cells (M) and tufted cells (T) to various areas in the OC for odor recognition and behavioral outputs.

1.2. Olfactory cortex

How does the OC receive the odor information from the OB? The M/T cells in the OB receive converging synaptic inputs from OSNs within each glomerulus and send the information to the OC. The OC is defined as the region which receives axons from the OB and includes anterior olfactory nucleus pars externa (AONpE), anterior olfactory nucleus pars principalis (AON), dorsal tenia tecta (dTT), ventral tenia tecta (vTT), ventral olfactory nucleus (VON), anterior piriform cortex (APC), olfactory tubercle (OT), posterior piriform cortex (PPC), nucleus of lateral olfactory tract (NLOT), anterior cortical amygdaloid nucleus (ACo), posterolateral cortical amygdaloid nucleus (PLCo), and lateral entorhinal cortex (LEC) (Neville and Haberly 2004; Murata et al., 2019) (Figure 2). The M/T cells in the OB send axonal projections to various areas of the OC in a specific pattern (Mori and Sakano, 2011; Neville and Haberly, 2004) (Figure 2). Both M and T cells project axons to only the anterior regions of the OC, including the AONpE, AON, APC, and OT. In contrast, the other regions of the OC receive inputs only from M cells. The “primary” OC often referred to the piriform cortex (PCx), which is located in the ventrolateral region of the forebrain, extends broadly along the anterior to posterior axis, and is composed of the APC and PPC. M cell axons in the OB projects to pyramidal cells in layer Ia of the PCx, a three-layered paleocortex (Haberly and Price,

1978). Anatomic tracing reveals that projections from the OB to the PCx are diffuse and overlapping with respect to inputs from a subset of glomeruli (Sosulski et al., 2011; Ghosh et al., 2011; Miyamichi et al., 2011). This diffuse projection patterns allow each principal pyramidal neuron in the PCx to gather inputs from different, possibly random, subsets of glomeruli, and activate ensembles of odor specificity of neurons distributed throughout the PCx (Stettler and Axel, 2009; Roland et al., 2017). The activated ensembles in the PCx encode the odor identity (Miura et al., 2012). The recent physiological study reveals that the odor coding in the PCx is different from that in the OB. The odor responses in the OB degrade when compared between the ketamine/ xylazine anesthesia state and the awake state while the PCx responses remain robust (Bolding et al., 2020).

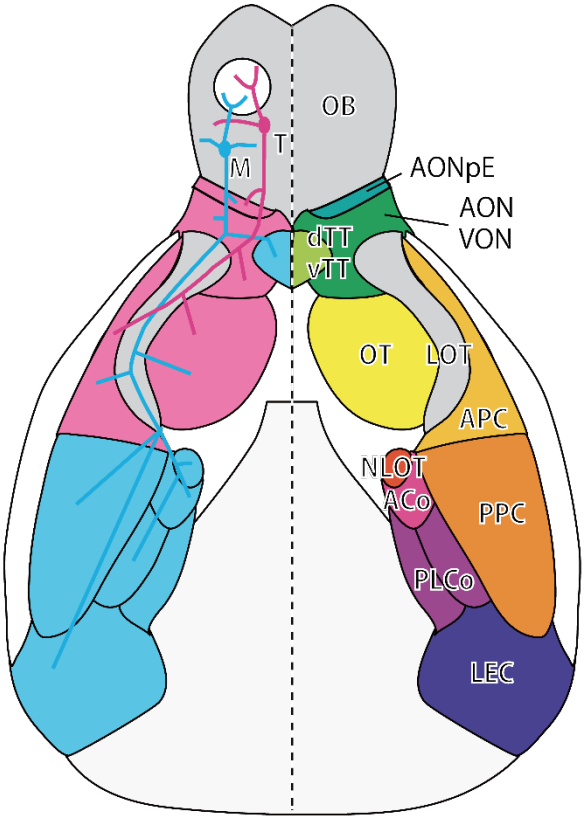

Figure 2 | Schematic diagrams showing the axonal projection of mitral and tufted cells and a variety of the olfactory cortex.

The left side diagram shows the axonal projection pattern of a single mitral cell (M) (blue) and a single tufted cell (T) (pink) to the OC. The OC receiving projections only from M cells are shown in blue, and the OC receiving projections from M cells and T cells are shown in pink. The right side diagram indicates various regions of the OC that receive axonal inputs from the OB. The OC is shown by the colored parts other than gray.

1.3.Ventral tenia tecta (vTT)

Despite growing knowledge on how odor molecules are coded by OSNs (Buck and Axel, 1991) and how neural circuits in the OB and OC process odor signals (Mori and Sakano, 2011; Mori et al., 2013; Wilson and Sullivan, 2011), our understanding of how distinct regions of the OC transform olfactory sensory information into behavioral outputs remains limited (Choi et al., 2011).

Physiological studies of the visual, auditory, and somatosensory cortices have revealed that neocortical sensory area neurons receive sensory signals from the environment, as well as top-down signals that are generated internally by higher-order cognitive and behavioral decision processes, including attention, reward-prediction, working memory, and behavioral choice processes (Allen et al., 2019; Gilbert and Sigman, 2007; Roelfsema and de Lange, 2016). In the OC, OT neurons encode goal-directed behaviors and exhibit enhanced odor responses when animals selectively attend to specific odors (Carlson et al., 2018; Gadziola and Wesson, 2016). Furthermore, c-Fos expression (a marker of neuronal activity) increases in different cells in the OT during distinct

motivated behaviors in mice (Murata et al., 2015). The APC plays important role for active maintenance in olfactory working memory (Zhang et al., 2019).

However, little is known how the OC encode the behavioral information signals. In the present study, we examined how the ventral tenia tecta (vTT), a relatively unexplored area of the OC located in the ventromedial aspect of the olfactory peduncle and received the top-down signals, transforms the perception of odor signals into reward-directed behaviors. The principal neurons of the vTT are the pyramidal cells, which receive bottom-up odor signals from the OB. Pyramidal cells are the principal neurons of the vTT and extend their apical tuft dendrites to the most superficial layer (layer Ia) of the cortex (Haberly and Price, 1978). These apical tuft dendrites receive excitatory synaptic inputs in layer Ia from the axon terminals of OB mitral cells (Friedman and Price, 1984; Igarashi et al., 2012; Nagayama et al., 2010) and excitatory synaptic inputs in layer Ib from Ib association fibers from other OC pyramidal cells (Luskin and Price, 1983a). These synaptic inputs to the apical tuft dendrites of layer I may convey olfactory sensory information directly from the OB, or indirectly after relay through olfactory cortical areas. In addition, vTT pyramidal cells extend their basal dendrites and proximal apical oblique dendrites into layers II and III, receiving top-down inputs from the medial prefrontal cortex (mPFC) (Hoover and Vertes, 2011) and higher-order areas of OC (Luskin and Price, 1983a) (Figure 3). In particular, the mPFC is involved in higher-order contextual encoding (Hyman et al.,2012; Shidara and Richmond, 2002) and preferentially fire at a specific position in the trajectory of a maze during a working memory task involving odor place-matching (Fujisawa et al., 2008). The firing of individual mPFC neurons tunes

to distinct task-elements that occurred in relation to the flow of goal-directed tasks, with each task-element occurring in a specific behavioral context (Lak et al., 2020). We therefore hypothesized that vTT neurons not only receive odor inputs from the OB, but are also influenced by top-down inputs generated in association with the higher cognitive and behavioral decision processes necessary for performing goal-directed behaviors (Buschman and Miller, 2014). To address the question of whether vTT neurons receive such top-down controls, we recorded the spike activity of individual vTT cells while mice performed a series of odor-guided, goal-directed behaviors.

We observed that the firing of individual vTT neurons during odor-guided goal-directed behaviors was highly tuned to distinct task-elements that occurred in relation to the flow of goal-directed tasks, with each task-element occurring in a specific behavioral context. Our results indicate that vTT functions are dynamic rather than fixed, whereby changes in information processing mode occur in a context-dependent manner during a sequence of feeding and drinking behaviors.

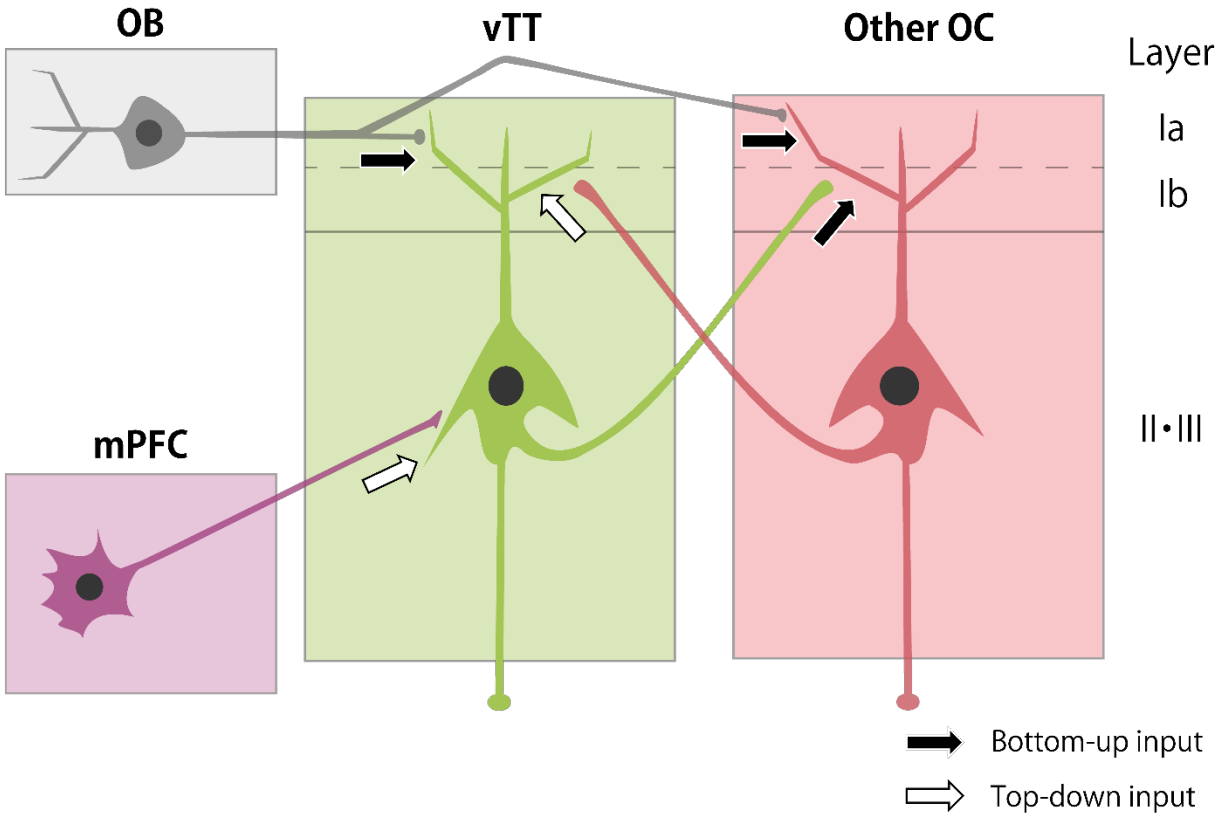

Figure 3 | Schematic overview showing the projection relashionship between the vTT and the other regions.

The vTT pyramidal cells receive olfactory sensory inputs including olfactory bulb afferent synapses terminating in layer Ia (gray) and association fiber synaptic inputs terminating in layer Ib (red) that are originated from other areas of the olfactory cortex. The vTT pyramidal cells also receive top-down inputs from mPFC (purple). The black arrows indicate the bottom-up inputs while the white arrows indicate the top-down inputs.

Chapter 2. Materials and Methods

2.1. Subjects

All experiments were performed on male C57BL/6 mice (9 weeks old; weighing 20–25 g) purchased from Shimizu Laboratory Supplies Co., Ltd. (Kyoto, Japan). Mice were individually housed in metal cages (13.5 × 23 × 17 cm) in a temperature-controlled environment with a 13-hr light/11-hr dark cycle (lights on at 8:00 and off at 21:00). Food and water were available ad libitum except during behavioral tasks. All experiments were performed in accordance with the guidelines for animal experiments at Doshisha University and with the approval of the Doshisha University Animal Research Committee.

2.2. Behavioral task

2.2.1. Apparatus for odor-guided go/no-go task

For the odor-guided go/no-go task, we used a behavioral apparatus controlled by the Bpod State Machine r0.5 (Sanworks LLC, NY, USA), an open-source control device designed for behavioral tasks. The apparatus comprised a custom-designed mouse behavior box (14 × 17 × 15 cm) with two nose-poke ports on the front wall. The box was enclosed within a soundproof box (BrainScience Idea. Co., Ltd., Osaka, Japan) equipped with a ventilator fan to provide adequate air circulation and low-level background noise. Each nose-poke port was equipped with a white light-emitting diode (LED) and infrared photodiodes. Interruption of the infrared beam generated a

transistor-transistor-logic (TTL) pulse, thus signaling the entry of the mouse head into the port. The odor delivery port was equipped with stainless steel tubing connected to a custom-made olfactometer (Uchida and Mainen, 2003). Eugenol and amyl acetate (Tokyo Chemical Industry Co., Ltd., Tokyo, Japan) were used as the go and no-go odor cues, respectively. These odors were diluted to 10% in mineral oil and further diluted 1:9 with airflow (1.8 L/min). Water reward delivery was based on gravitational flow, controlled by a solenoid valve (The Lee Company, CT, USA), and connected via Tygon tubing to stainless steel tubing. The reward volume (6 μL) was determined by the duration of opening of the solenoid valve and was regularly calibrated.

For the odor-guided go/no-go task, mice (n = 6) were placed on a water restriction schedule of 1–2 mL/day with daily body weight monitoring to ensure that their body weight remained within 80% of their body weight prior to restriction.

2.2.2. Apparatus for odor-guided eating/no-eating task

For the odor-guided eating/no-eating task, mice (n = 6) were placed on a food restriction schedule of 3-4 g/day with daily body weight monitoring to ensure that their body weight remained within 80% of their body weight prior to restriction. During the training sessions, mice learned to associate odors with a sucrose reward. Training was conducted in a plastic cage (38.5 × 33.5 × 18 cm, CLEA Japan Inc., Tokyo, Japan) which contained virgin pulp bedding (SLC, Inc., Shizuoka, Japan). The cage was monitored with a recording camera in a soundproof room with a ventilator fan that provided air circulation and a low-level of background noise. Mice were presented with 1-2 g of

granulated sugar on a Petri dish with holes which contained a filter paper (2×2 cm) soaked with odor (40 μL). The dish was covered with bedding at an arbitrary position in the cage. The odor cues were eugenol (Tokyo Chemical Industry Co., Ltd., Tokyo, Japan) and vanilla essence (NARIZUKA Corporation, Tokyo, Japan), diluted to 10% in mineral oil.

2.3. Surgery

Mice were anesthetized with medetomidine (0.75 mg/kg i.p.), midazolam (4.0 mg/kg i.p.), and butorphanol (5.0 mg/kg i.p.), and implanted with a custom-built microdrive of three or four tetrodes in the vTT (2.6 mm anterior to bregma, 0.4 mm lateral to the midline, 4.0 mm from the brain surface). Individual tetrodes consisted of four twisted polyimide-coated tungsten wires (California Fine Wire, single wire diameter 12.5 μm, gold-plated to less than 500 kΩ). The tips and sides of the tetrodes were coated with DiI (Molecular Probes, OR, USA). Two additional screws were threaded into the bone above the cerebellum for reference.

2.4. Electrophysiological recordings

2.4.1. Electrodes for extracellular recordings

The electrodes were connected to an electrode interface board (EIB-18, Neuralynx, MT, USA) on a microdrive. A microdrive array was fixed to the skull with LOCTITE 454 (Henkel Corporation, Düsseldorf, Germany). After the completion of surgery, mice received atipamezole (0.75 mg/kg i.p.) to reverse the effects of medetomidine and enable a shorter recovery period. Analgesics were

administered post-surgery (ketoprofen, 5 mg/kg, i.p.). Behavioral training resumed at least 1 week after surgery.

Electrical signals were obtained with either a Cheetah recording system (Neuralynx) or open-source hardware (Open Ephys). For unit recordings, signals were sampled at 32 kHz in NeuraLynx or 30 kHz in Open Ephys and band-pass filtered at 600–6,000 Hz. After each recording, tetrodes were lowered by 20, 40, or 75 μm more by turning a screw of the microdrive to obtain new units.

2.4.2. Spike sorting and screening criteria of units

All data analyses were performed using built-in software in MATLAB 2019a (The Mathworks, Inc., MA, USA). Spikes were sorted into clusters offline based on their waveform energy, peak amplitudes, and first principal components from the four tetrode channels using an automated spike-separation algorithm KlustaKwik (K.D. Harris). Resulting classifications were corrected and refined manually with MClust software (A.D. Redish) (Figure 4). Clusters were considered single units only when the following criteria were met: (1) refractory period (2 msec) violations were less than 0.2% of all spikes and (2) isolation distance, estimated as the distance from the center of the identified cluster to the nearest cluster based on the Mahalanobis distance, was more than 20. To examine the behavioral correlates of vTT cell firing patterns, we selected vTT cells with average firing rates during the trials that were greater than 0.3 Hz for further analyses.

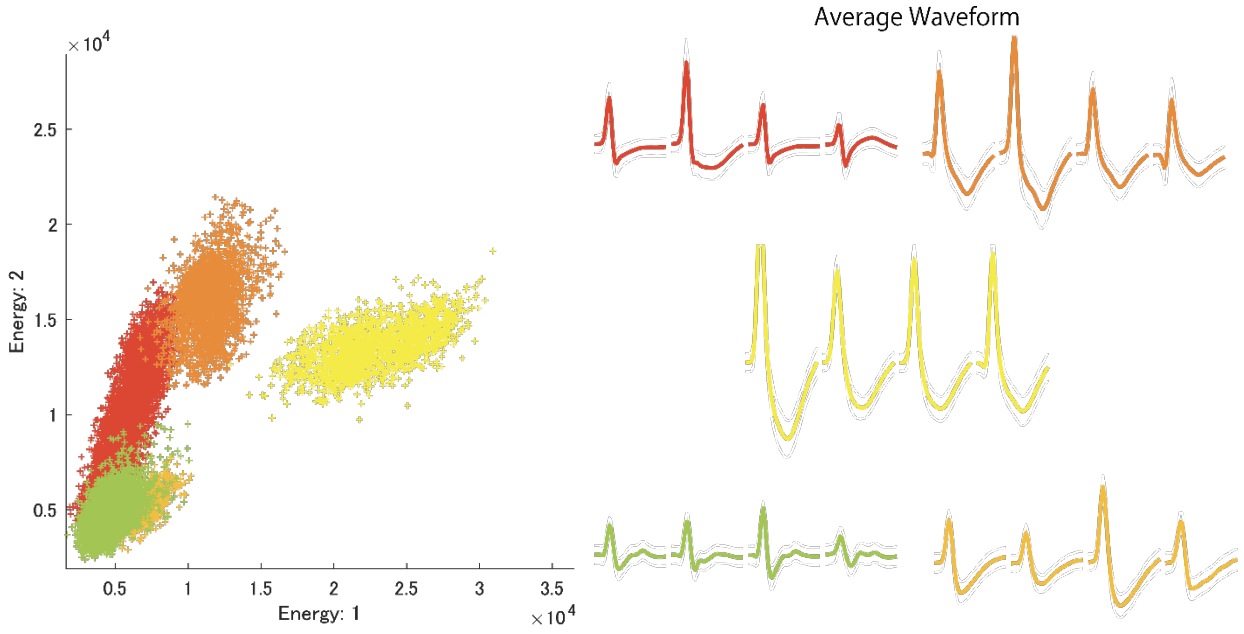

Figure 4 | Clustering of single-neuron responses from the recorded data.

The left panel shows five single-neurons identified from a tetrode. Clusters, represented by different colors, indicate different single-neurons. The right panel indicates the average spike waveform of the five identified single-neurons. The colors correspond to those of the clusters.

2.4.3. Histology

After recording, mice were deeply anesthetized with intraperitoneal injection of sodium pentobarbital. Electric lesions were induced using 10–20 μA direct current stimulation for 5 sec using one of the four tetrode leads. Mice were perfused transcardially with phosphate-buffered saline (PBS) followed by 4% paraformaldehyde (PFA). Brains were removed from the skull and post-fixed in PFA. Brains were sliced into 50-μm-thick coronal sections. The electrode tracks were first assessed by tracking the fluorescence of DiI. After staining with cresyl violet, electrode tracks and recording positions were determined in reference to the mouse brain atlas developed by Paxinos and Watson (Paxinos, 2004).

2.5. *In situ* hybridization

Adult male mice (n=3) were used. Digoxigenin-(DIG)-labeled RNA probes for *Slc17a7* and *Gad1/2* were generated using an in vitro transcription kit (Roche, Basel, Switzerland), according to the manufacturer's protocol using plasmids generously provided by Drs. Katsuhiko Ono and Yuchio Yanagawa (Asada et al., 1997; Makinae et al., 2000; Ono et al., 2008). Brain sections (20-μm-thick) were mounted on glass slides (CREST, Matsunami, Osaka, Japan) using a paintbrush and dried overnight in a vacuum desiccator. The dried sections were then fixed in 4% PFA, digested with Proteinase K (10 μg/mL) for 30 min, and post-fixed in 4% PFA. After prehybridization, the sections were incubated overnight at 65°C with DIG-labeled RNA probes. After stringent washing, sections were blocked with 1% blocking reagent (11096176001, Roche) in TNT for 1 h. Subsequently, sections were incubated overnight at 4°C with alkaline phosphatase-conjugated anti-DIG antibody (1:1,000; Roche). Sections were then washed three times in TNT and once in TS 8.0 (0.1 M Tris-HCl, pH 8.0, 0.1 M NaCl, 50 mM MgCl2). Finally, alkaline phosphatase activity was detected using an HNPP fluorescence detection set (11758888001, Roche), according to the manufacturer's instructions. After three 30-min incubations, sections were washed with PBS. Finally, sections were counterstained with NeuroTrace green (Thermo Fisher Scientific, MA, USA) and mounted in PermaFluor (Thermo Fisher Scientific).

2.6. Retrograde tracing

Adult male mice were anesthetized with medetomidine (0.75 mg/kg i.p.), midazolam (4.0 mg/kg i.p.), and butorphanol (5.0 mg/kg i.p.), and then placed in a stereotaxic apparatus (SR-5M, Narishige, Tokyo, Japan). Injections were conducted with a syringe pump (UltraMicroPump III, WPI, FL, USA) connected to a Hamilton syringe (RN-1701, Hamilton, Nevada, USA) and a mounted glass micropipette with 50 μm tip diameter connected to the syringe with an adaptor (55750-01, Hamilton).

CTB conjugated with Alexa 555 (Thermo Fisher Scientific) was unilaterally or bilaterally injected (300 nL at 100 nL/min) into the medial prefrontal cortex (mPFC) (A/P, 2.4 mm; M/L, 0.4 mm from bregma; D/V, 1.0 mm from the brain surface; n = 3 from 2 mice), olfactory bulb (OB) (A/P, 4.3 mm; M/L, 0.8 mm from bregma; D/V, 1.5 mm from the brain surface; n = 3 from 2 mice), anterior olfactory nucleus (AON) (A/P, 2.8 mm; M/L, 1.3 mm from bregma; D/V, 2.6 mm from the brain surface; n = 3 from 2 mice), olfactory tubercle (OT) (A/P, 1.5 mm; M/L, 1.0 mm from bregma; D/V, 4.7 mm from the brain surface; n = 5 from 3 mice), anterior piriform cortex (APC) (A/P, 2.3 mm; M/L, 1.8 mm from bregma; D/V, 3.4 mm from the brain surface; n = 4 from 4 mice), or posterior piriform cortex (PPC) (A/P, -1.5 mm; M/L, 3.6 mm from bregma; D/V, 4.5 mm from the brain surface; n = 3 from 2 mice), or ventral tenia tecta (vTT) (250 nL; A/P, 0.3 mm tilted 30°; M/L, 0.4 mm from bregma; D/V, 4.6 mm from the brain surface; n = 3 from 2 mice). After surgery, mice received atipamezole (0.75 mg/kg i.p.) and ketprofen (5 mg/kg, i.p.). One week later, mice were deeply anesthetized and perfused with saline followed by 4% PFA under anesthesia.

Brains were sliced into 50-μm-thick coronal sections. Density was measured by delineating an outline of nuclear stained cells using Image J and represented as mm^2.

2.7. Analysis

2.7.1. Spike train analysis

In the odor-guided go/no-go task, neural and behavioral data were synchronized by inputting each event timestamp from the Bpod behavioral control system into the electric signal recording system. To calculate firing rates during tasks, peri-event time histograms (PETHs) were calculated using a 20 msec bin width and smoothed by convolving spike trains with a 60 msec wide Gaussian filter (Figure 5). In the odor-guided eating/no-eating task, timestamps were acquired for each event (onset of dish approach, initial dish contact, and dish removal) from frames of recorded behavioral videos, which were synchronized to spike data. To calculate cell firing rates during tasks, PETHs were calculated using a 500 msec bin width and smoothed by convolving spike trains with a 500 msec wide Gaussian filter (Figure 6).

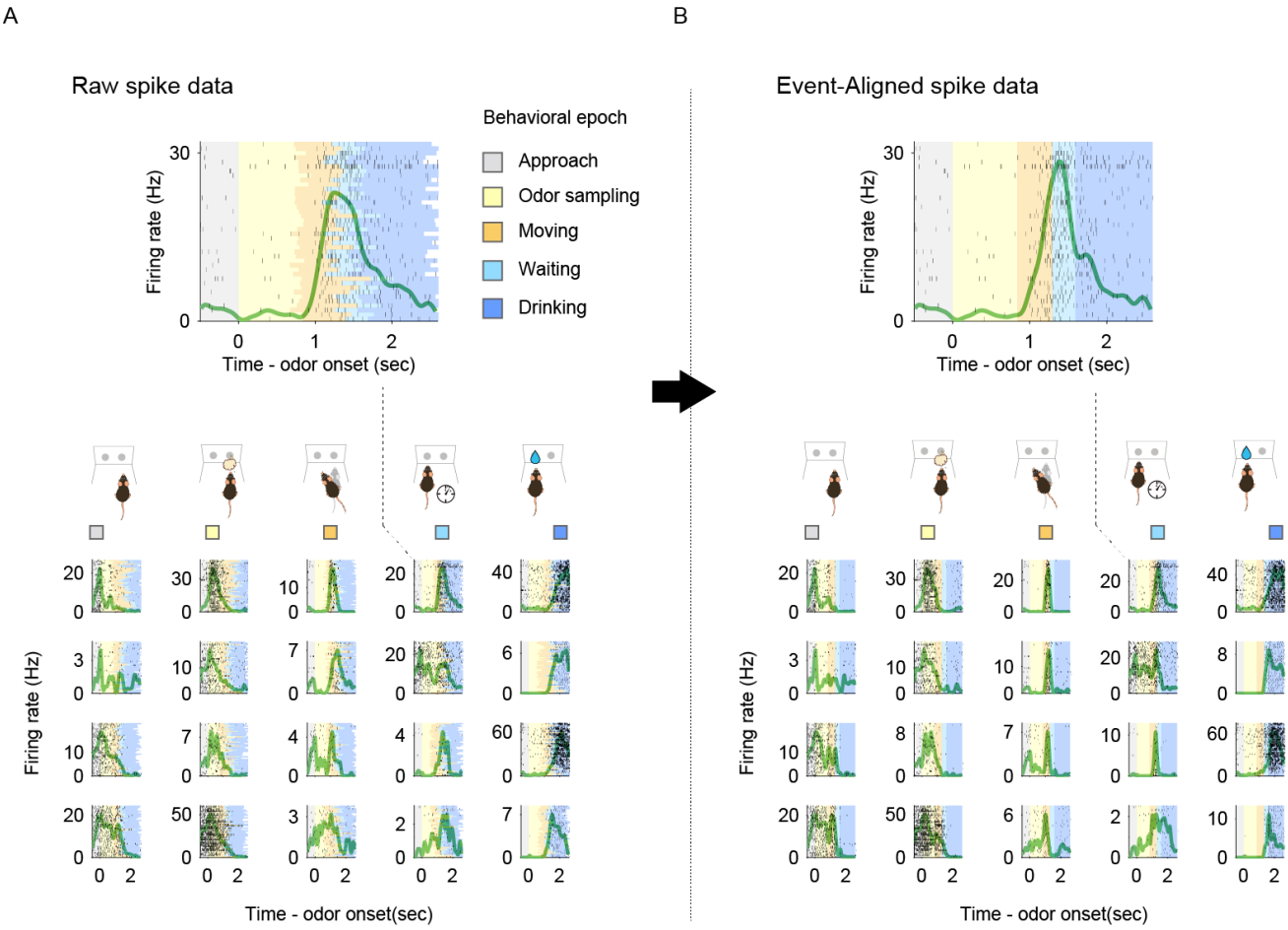

Figure 5 | Representative activity patterns of behavior-specific active vTT cells in the odor-guided go/no-go task.

(A) Examples of spike data tuned to specific behaviors. Spike histograms (green line) were calculated using a 20 msec bin width and smoothed by convolving spike trains with a 60 msec wide Gaussian filter. Gray shading indicates the approach epoch (500 msec before odor port entry), yellow shading indicates the odor-sampling epoch (from entry into the odor port to exiting the odor port), orange shading indicates the moving epoch (from exiting the odor port to entry into the water port), light blue shading indicates the waiting epoch (water reward delay, 300 msec before water valve was turned on), and blue shading indicates the drinking epoch (1,000 msec after the water valve was turned on).

(B) Same as (A) for event-aligned spike data, derived by linearly scaling time intervals between behavioral epochs in each trial to the median interval across correct go trials. Numbers of spikes between epochs are preserved. Data presented are from the same cells and in the same order as those in (A).

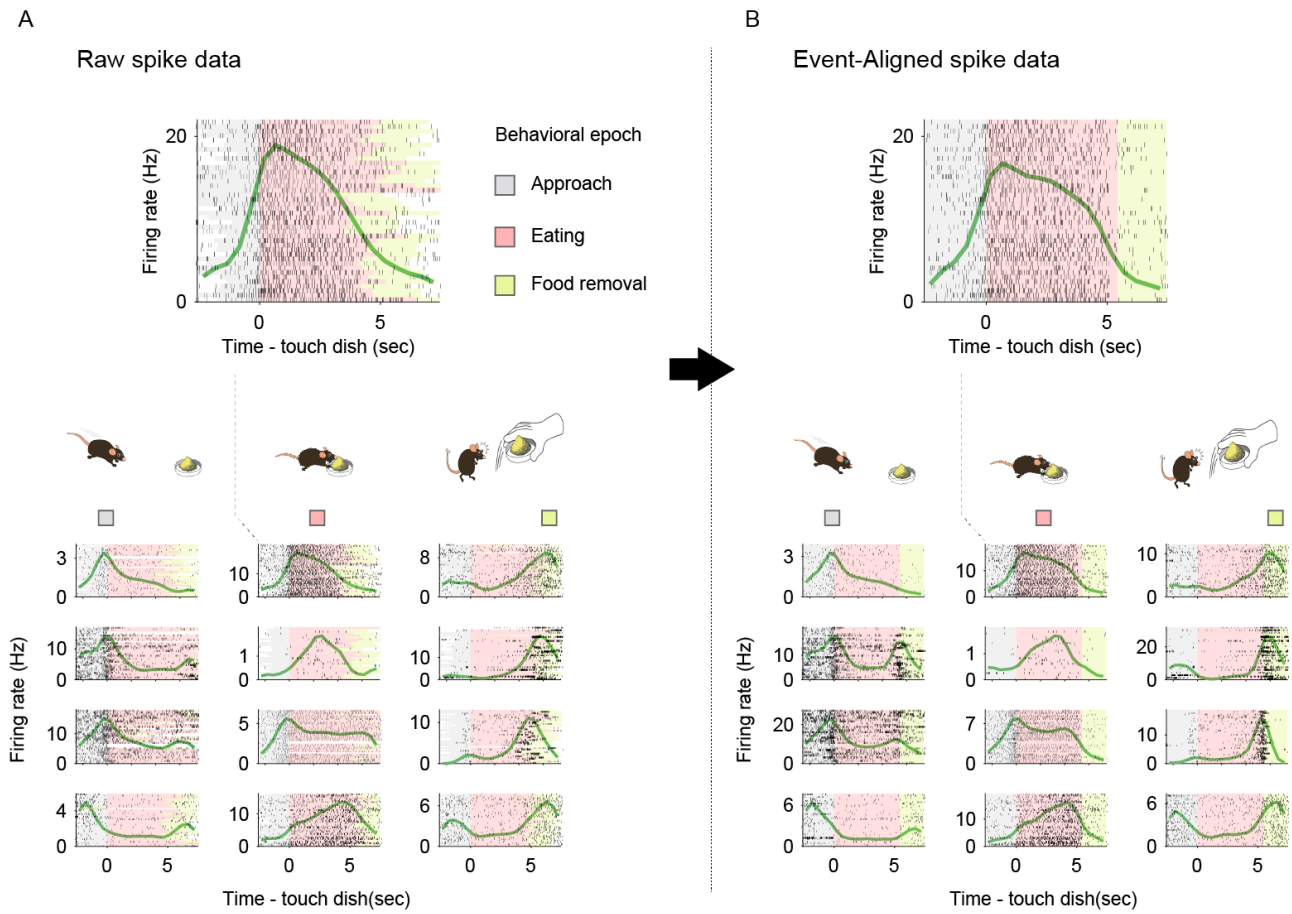

Figure 6 | Representative activity patterns of behavior-specific active vTT cells in the odor-guided eating/no-eating task.

(A) Examples of spike data tuned to specific behaviors. Spike histograms (green line) were calculated using a 500 msec bin width and smoothed by convolving spike trains with a 500 msec wide Gaussian filter. Gray shading indicates the approach epoch (from the start of approach behavior to contacting the dish), pink shading indicates the eating epoch (from the start of eating behavior to food removal), light green shading indicates the food removal epoch (2 sec after food removal).

(B) Same as (A) for event-aligned spike data, derived by linearly scaling time intervals between behavioral epochs in each trial to the median interval across eating trials. Numbers of spikes between epochs are preserved. Data presented are from the same cells and in the same order as those in (A).

2.7.2. Event-aligned spike histograms

To examine the relationship between firing rate changes among individual vTT cells and the development of behavioral epochs in behavioral tasks, EASHs were generated (Ito and Doya, 2015). As behavioral epoch durations varied for each trial, median epoch durations were first calculated. In the odor-guided go/no-go task, the median duration of odor sampling epochs (from the onset of the go odor cue to exiting the odor port) was 839 msec, and the median duration of moving epochs (from odor port exit to water port entry) was 455 msec. Spike timing during each epoch and for each trial was linearly transformed to correspond with the median duration of each behavioral epoch. The number of spikes in each epoch was preserved. We defined the approach epoch (500 msec before odor port entry), waiting epoch (300 msec reward delay, from entry into the water port to the onset of water reward), and drinking epoch (1,000 msec after the onset of the water reward). These epochs were not applied to the transformation because their durations did not change across trials. In this manner, a regular raster plot was transformed into event-aligned raster plots (Figure 5B). An EASH was subsequently calculated using a 20 msec bin width and smoothed by convolving spike trains with a 60 msec wide Gaussian filter from the raster plot.

In the odor-guided eating/no-eating task, the median duration of the approach epoch (from the start of approach behavior to contacting the dish) was 2.57 sec, and the median duration of the eating epoch (from the start of consumption to food removal) was 5.44 sec. Spike timing during each epoch of each trial was linearly transformed into a corresponding median duration for each epoch. The number of spikes in each epoch was preserved. We defined the food removal epoch (2 sec after the start of food removal), which was not applied to this transformation because

the duration of this epoch did not change across trials. Thus, regular raster plots were transformed into event-aligned raster plots (Figure 6B). An EASH was subsequently calculated using a 500 msec bin width and smoothed by convolving spike trains with a 500 msec wide Gaussian filter from the raster plots.

2.7.3. ROC analysis

To quantify firing rate changes, we used an algorithm based on ROC analysis that calculates the ability of an ideal observer to classify whether a given spike rate was recorded in one of two conditions (e.g., during go or no-go odor cue presentation) (Felsen and Mainen, 2008). We defined an auROC equal to 2 (ROC area – 0.5), with the measure ranging from –1 to 1, where –1 signified the strongest possible value for one alternative and 1 signified the strongest possible value for the other.

The statistical significance of ROC analysis was determined using a permutation test. For this test, ROC curves were recalculated after all firing rates were randomly assigned to either of the two groups (e.g., go-cue trial group and no-go-cue trial group) arbitrarily. This procedure was repeated a large number of times (500 times for all analyses) to obtain a distribution of values. The fraction of random values exceeding the actual value was then calculated. Based on this quantification, the auROC value for each cell was calculated along with a time course for the go/no-go or eating/no-eating tasks in sliding windows (in overlapping 100 msec windows starting every 20 msec for the go/no-go task and overlapping 500 msec windows starting every 100 msec

for the odor-guided eating/no-eating task). The auROC values during the go or no-go trials were then calculated by quantifying firing rate changes from baseline. A similar procedure was employed for the eating trials by quantifying firing rate changes from baseline and for go trials by quantifying firing rate changes relative to no-go trials. For all analyses, significance was tested with $\alpha = 0.01$. Only cells with a minimum number of 10 trials for each analyzed condition were included in these analyses.

2.7.4. Evaluation of neural tuning to specific behaviors

To determine the timepoint at which each vTT cell increased its firing rate the most and the duration of increased firing during the task, two measures were calculated from each auROC value (Figure 7):

(1) Tuning peak time: the time corresponding to the peak of the significant points when a cell significantly increased its firing rate from baseline for five or more consecutive bins ($p < 0.01$, permutation test)

(2) Tuning duration: the duration, including the tuning peak time, for which increased firing was significant ($p < 0.01$, permutation test)

In the odor-guided go/no-go task, we classified vTT cells with tuning peak times (n = 217 cells) into five groups based on the epoch in which tuning peak time occurred during correct go trials. Of these, 7% of all cells had tuning peak times in the approach epoch, 24% in the

odor-sampling epoch, 23% in the moving epoch, 11% in the waiting epoch, and 15% in the drinking epoch.

In the odor-guided eating/no-eating task, we classified vTT cells with tuning peak times (n = 192 cells) into three groups based on the epoch in which tuning peak time occurred during the eating trials. In total, 19% of all cells had tuning peak times during the approach epoch, 20% during the eating epoch, and 12% during the food removal epoch.

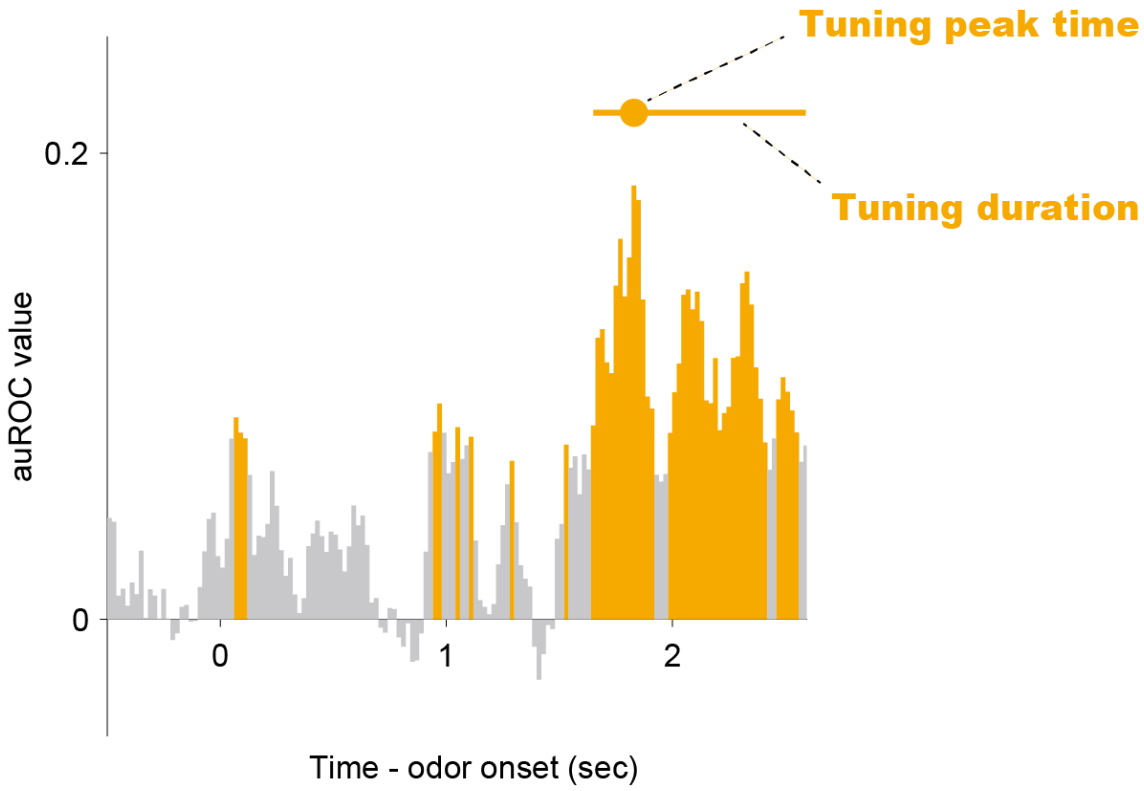

Figure 7 | Tuning peak time and tuning duration.

To determine the timepoint at which a vTT cell increased its firing rate the most and the duration of this increased firing during the task, we calculated "tuning peak time" (orange dot) and "tuning duration" (orange horizontal line) from the auROC values (see Materials and methods). Orange bars indicate significant increases from baseline. Gray bars indicate neither significant increases nor decreases.

2.7.5. Relative distributions of significant responses

The distribution of behavioral epoch-specific firing for each cell type was calculated as follows (Figure 8). First, for each cell group, the number of cells with significant excitatory (or suppressed) firing during each time bin for each task was calculated. Their distribution was estimated using Gaussian kernel smoothing via the fitdist function in MATLAB with a bandwidth of 100 msec in the odor-guided go/no-go task and 500 msec in the odor-guided eating/no-eating task. Second, the distribution of the significant excitatory (or suppressed) firing was compared with the cell-shuffled data for each cell group. To calculate the 99% confidence intervals of this distribution, we ran 1,000 iterations in which cellular group identities were randomized. We then calculated the distribution of significant excitatory (or suppressed) firing of each cell group, as above. For each bin in the tasks, the edges of the confidence interval were at the 0.5th and 99.5th percentiles of the distribution, as calculated from the cell-shuffled data (gray shaded area in Figure 8C). The significance of activity patterns for each cell group was determined by comparing the standard deviations of the data with those obtained from the cell-shuffled data, in which shuffling was performed 1,000 times by randomizing the cell selection.

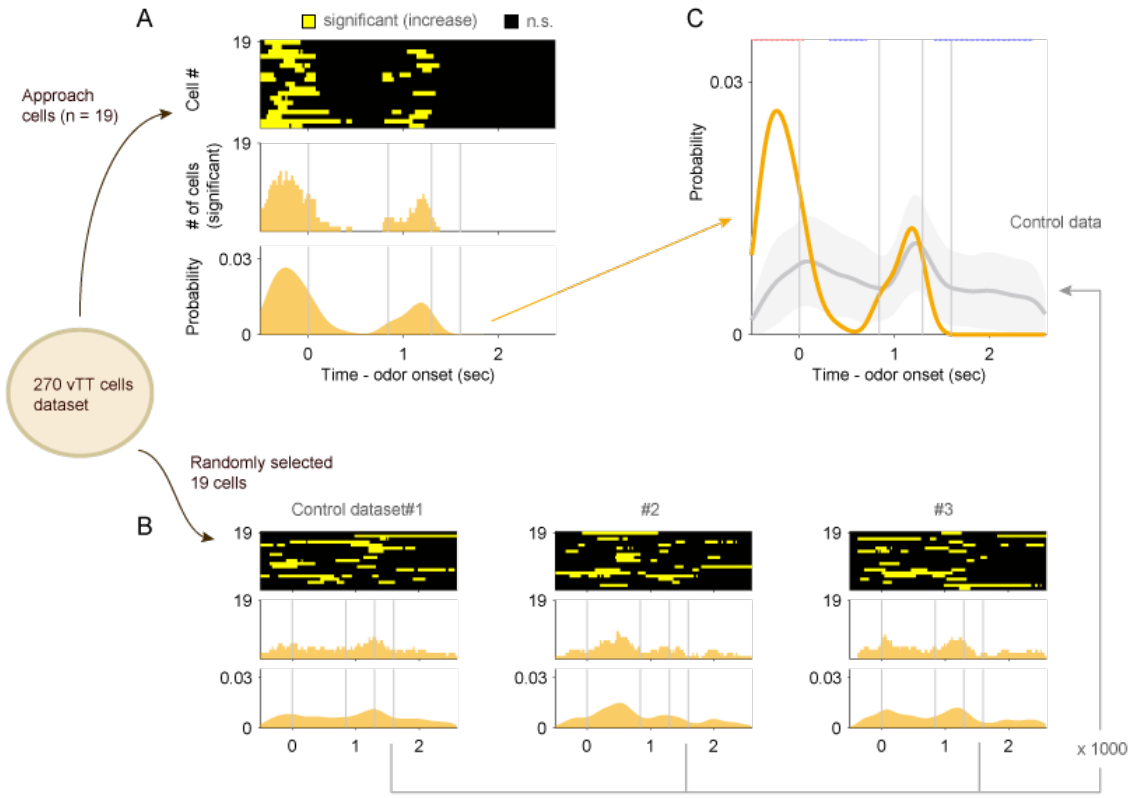

Figure 8 | Relative distribution of significant responses.

(A) Relative distribution of significant excitatory firing of the cell group involved in approach. The number of cells with significant excitatory firing (top yellow boxes, significant increase from baseline; black boxes, not significant) during each time bin was quantified (middle histogram). Their distribution was estimated using Gaussian kernel smoothing (bottom-shaded area).

(B) Comparison of (A) with the cell-shuffled data. We ran 1,000 iterations in which cellular group identities were randomized and calculated the distribution of significant excitatory firing by each cell group, as in (A).

(C) The significance of activity patterns for the cell group involved in approach (orange line) was determined by comparing the standard deviations of the data with those obtained from the cell-shuffled data (gray line and gray shaded area). Red dots indicate that a time bin contained more cells with significant responses than that in the distribution of the cell-shuffled data. Blue dots indicate that a time bin contained fewer cells with significant responses than that in the distribution of the cell-shuffled data. Vertical gray lines indicate transitions between behavioral epochs.

2.7.6. SVM decoding analysis

A support vector machine (SVM) algorithm with a linear kernel as a classifier (Cury and Uchida, 2010; Miura et al., 2012) and a Matlab function (fitcsvm) were used for analysis. All analyses were conducted on trial data pooled across animals. A matrix containing concatenated firing rates for each trial and each cell was the input for the classifier. The matrix dimensions were the number of cells by the number of trials. To avoid over-fitting, k-fold cross-validation (k = 10) was used to calculate the decoding accuracy of trial type discriminations. To compute decoding accuracy, 40 trials for each trial type (from the start of the session) were selected as the data set. Next, the data set was partitioned into ten equal parts; one part was used for testing, and the remaining parts were used for training the classifier. This process was repeated ten times to test each individual part. The mean value of the accuracy was then used for decoding accuracy. To compute the decoding accuracy of a 100 msec bin window (step: 20 msec), the classifier was trained and tested with a 100 msec bin window (step: 20 msec). In order to verify the statistical significance of the computed accuracy, we estimated the accuracy distribution on label-shuffled data using 1,000 repetitions of a random selection from the data set.

2.7.7. Statistical analysis

Data were analyzed in Matlab 2019a. Statistical methods for each analysis are described above, in the results section, or in the figure legends. The Tukey-Kramer method was applied for significance tests with multiple comparisons. Although sample sizes in this study were not pre-determined with

sample size calculations, they were based on previous research in the olfactory cortex field (Manabe et al., 2011; Miura et al., 2012). Randomization and blinding were not employed. Biological replicates for the histological studies are described in the figure legends.

Chapter 3. Results

3.1. Activity of vTT cells during the odor presentation phase of the odor-guided go/no-go task

3.1.1. Behavioral paradigms and indexes during the odor-guided go/no-go task

To examine how ventral tenia tecta (vTT) cell firing changes in relation to odor-guided, goal-directed behaviors, we recorded the neural activity of vTT cells during an odor-guided go/no-go task with a water reward (Figure 9). In this task, a light stimulus presented at the right odor port signaled to a water-restricted mouse to start the task and insert its nose into the odor port. At the moment of the nose poke, an odor cue was presented for 500 msec in the odor port. The mouse was required to keep its nose in the odor port during odor presentation to sniff the odor cue. After odor presentation, the light was turned off, and the mouse could withdraw its nose from the odor port. If the go odor cue (eugenol) was presented, the mouse was required to move to and poke its head into the left water port within a timeout period of 2 sec to obtain a water reward (go trial). At the water port, the mouse was required to keep its head in the port for 300 msec to wait for water delivery. A drop of water (6 μL) was delivered 300 msec after the head poke. If the no-go odor cue (amyl acetate) was presented, the mouse was required to stay near the odor port for 2 sec after the end of odor delivery without poking its head into the water port (no-go trial). After the mice were well trained, their behavioral accuracy remained above 80% throughout the session. The median duration of nose pokes after the onset of odor stimulation was 839 msec (interquartile range:

703-1,003 msec) in the go trials and 738 msec (interquartile range: 621-946 msec) in the no-go trials (57 sessions from six mice).

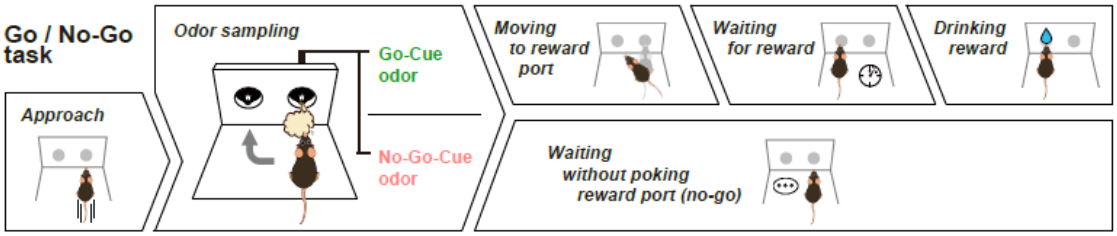

Figure 9 | Schematic of the odor-guided go/no-go task.

Behavioral epochs progressed temporally from left to right.

3.1.2. Firing patterns of the vTT neurons during the odor-guided go/no-go task

We recorded the spiking activity of 270 vTT cells from six mice (Tables 1 and 2; recording positions are shown in Figure 10) while they performed the go/no-go task. As the vTT receives direct inputs from mitral and tufted cells of the olfactory bulb, we first focused on whether vTT cells exhibited odor cue-responsive activity during odor presentation. We observed that a subset of vTT cells increased their firing rates during the odor presentation phase during both go and no-go trials (an example is shown in Figure 11).

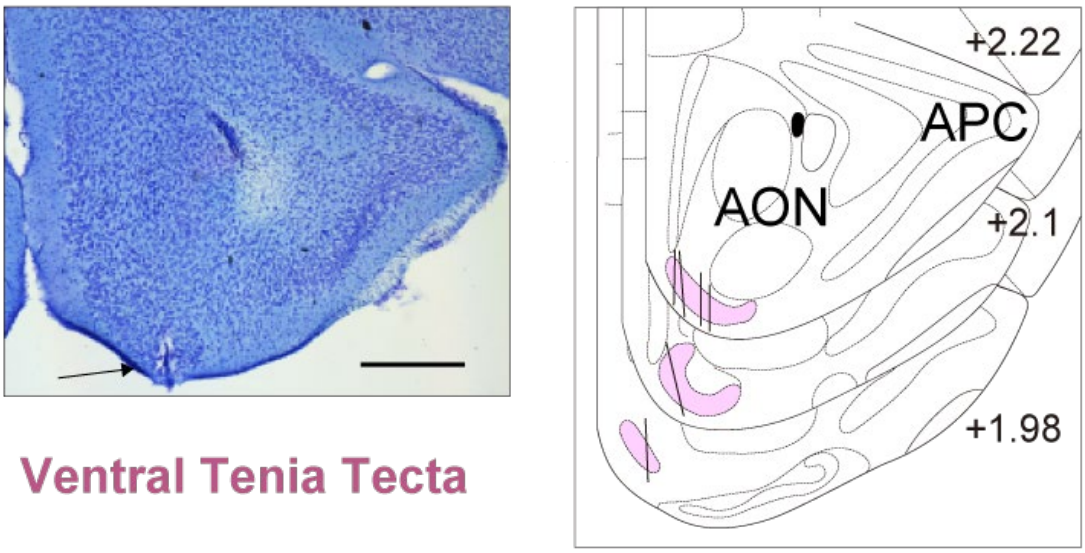

Figure 10 | The distribution of recording positions of the vTT in the odor-guided go/no-go task.

Nissl-stained frontal sections (arrow in the left panel indicates recording track) and recording tracks (vertical thick lines) of the vTT in the odor-guided go/no-go task. The pink area in the right panel shows layer II of the vTT. APC, anterior piriform cortex; AON, anterior olfactory nucleus. Scale bar: 500 μm.

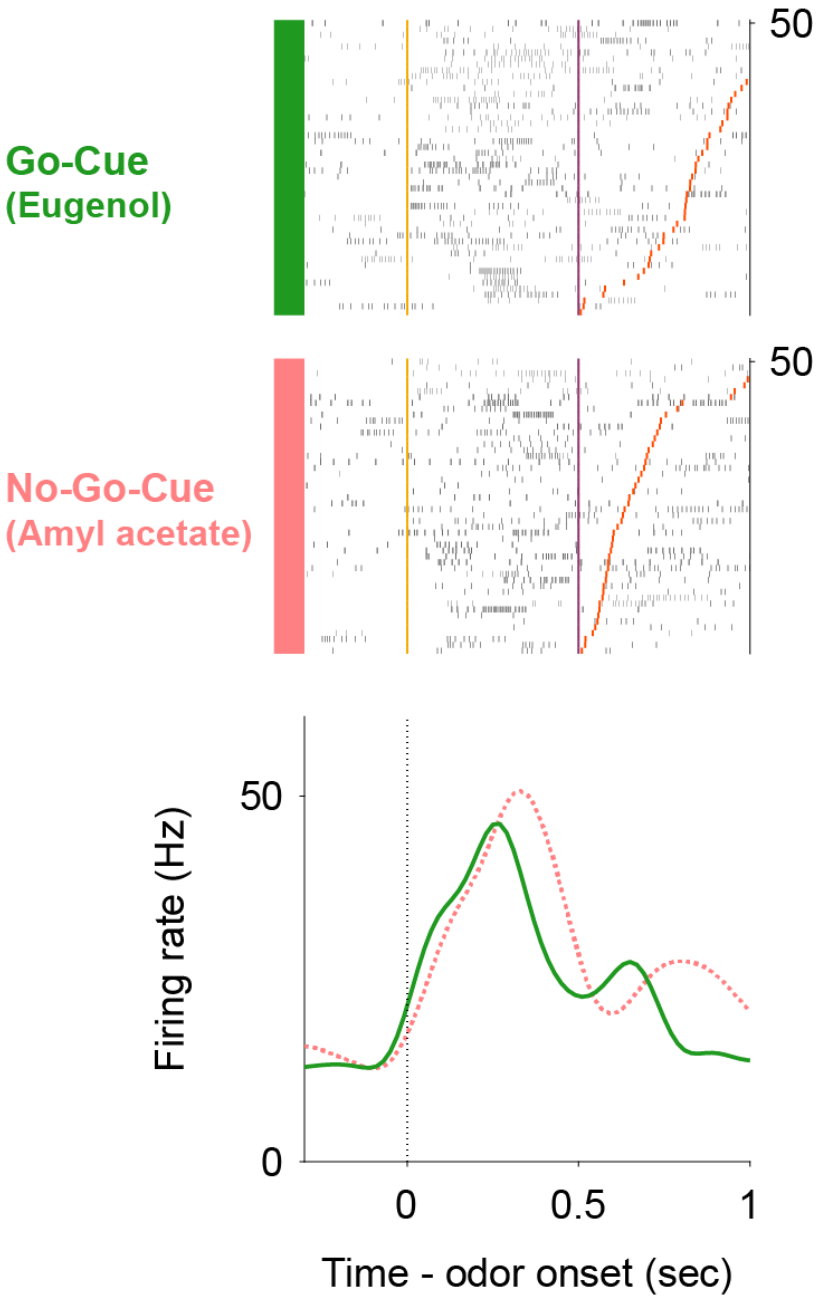

Figure 11 | Example firing patterns of vTT cells during the odor-guided go/no-go task.

Each row contains spikes (black ticks) for one trial, aligned to the time of odor valve opening (corresponding to odor port entry, orange ticks). Purple and red ticks indicate times of odor valve closing and odor port exits, respectively. Correct trials are grouped by odor. Within each group, correct trials are sorted by the duration of the odor sampling epoch (the time from odor valve opening to odor port exit). Histograms (green: Go Cue and pink: No-Go-Cue) are averaged across odors, calculated using a 20 msec bin width, and smoothed by convolving spike trains with a 60 msec-wide Gaussian filter. The vertical dashed line indicates the time of odor valve opening.

Table 1 | Basic information in the odor-guided go/no-go task

Mouse	Recording sessions	Trials /session	Go trials /session	No-Go trials /session	Recorded cells /session
#1	5	380±31	190±16	190±15	3±1
#2	8	453±27	227±14	226±13	6±2
#3	5	435±44	217±22	217±22	4±1
#4	14	464±21	233±10	231±10	7±1
#5	13	321±24	161±12	160±12	3±0
#6	10	443±24	222±12	222±12	5±1

Table 2 | The distribution of the vTT cell groups in the odor-guided go/no-go task

Mouse	Approach cells	Odor sampling cells	Moving cells	Waiting cells	Drinking cells	Others	(Total)
#1	0	10	1	0	2	0	13
#2	6	8	13	7	10	4	48
#3	0	5	7	1	2	3	18
#4	6	21	15	11	18	32	103
#5	3	8	16	5	1	7	40
#6	4	14	11	5	7	7	48
(Total)	19	66	63	29	40	53	270

3.1.3. vTT cell activity patterns during the odor presentation phase of the odor-guided go/no-go task

To quantify the dependence of firing rate on the odor presentation phase, we calculated firing rate changes from baseline (pre-odor cue period, 1.2 to 1 sec before the odor port entry) in sliding bins (width, 100 msec; step, 20 msec) using a receiver operating characteristic (ROC) analysis approach. We calculated the area under the ROC curve (auROC) at each time bin (spike data were aligned to the onset of odor valve opening). auROC values ranged from -1 to +1, with positive and negative values reflecting increased and decreased firing rates relative to baseline, respectively. We further determined auROC value significance using a permutation test (see Materials and methods).

Using the auROC approach, we defined the odor cue-responsive population (n = 68 cells, 25% of the recorded cells) as cells that significantly increased their firing rates from baseline for five consecutive bins (100 msec) during the odor presentation phase (500 msec after the odor valve opening) in correct go or no-go trials. Across all the cells, many exhibited significant increases in firing rate relative to both the go and no-go odor cue presentation phases (top color maps in Figure 12A, $p < 0.01$, permutation test). No significant differences in the magnitude of these increases between the go and no-go odor cue phases at each time point were observed (bottom lines in Figure 12A, $p > 0.01$, Welch's t test). Changes in firing rate in individual vTT cells exhibited similar time courses for go and no-go trials. We quantified this by calculating the correlation coefficients of response profiles between correct go trials and correct no-go trials for each cell (top lines in Figure 12B). This analysis revealed that the activity of vTT cells was strongly correlated between go and

no-go odor cue presentation phases, whereas different cell pairs did not exhibit this correlation (bottom lines in Figure 12B, $p < 10^{-13}$, two-sample Kolmogorov–Smirnov test). These results suggest that individual vTT cells did not represent odor cue differences between go and no-go trials during odor presentation phases. We therefore hypothesized that firing activity mainly reflected animal behavior and was dependent on task context.

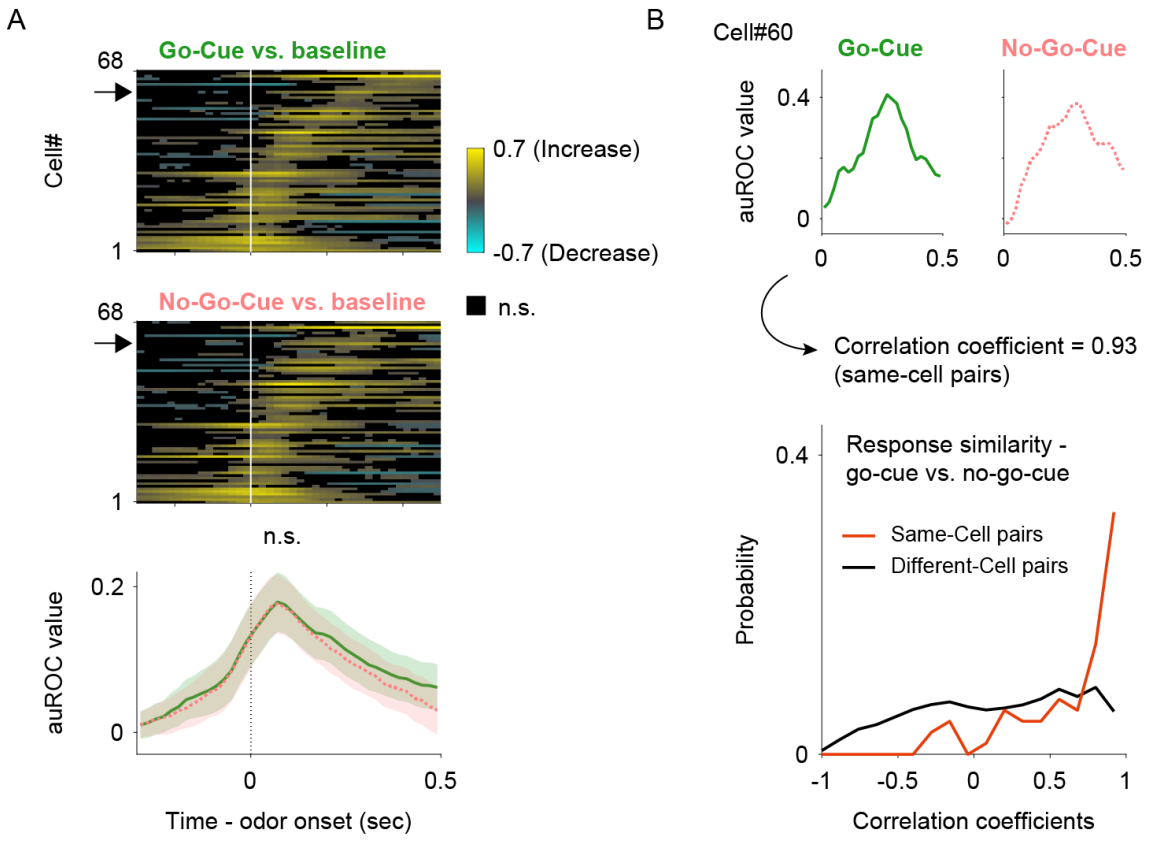

Figure 12 | vTT cell activity patterns during the odor presentation phase of the odor-guided go/no-go task.

(A) Upper panels: auROC values for cells with significantly higher firing rates than baseline (n = 68 cells) during the odor presentation phase (upper, go trials; lower, no-go trials). Each row corresponds to one cell, with cells in both graphs presented in the same order. auROC values (aligned by odor valve opening) were calculated by comparing go odor cue presentation and baseline (pre-cue odor period, 1.2 to 1 sec before the odor port entry) or no-go odor cue presentation and baseline in sliding bins (width, 100 msec; step, 20 msec).

Cells were sorted by peak value times of auROC values calculated by comparing go odor cue presentation and baseline for each cell. Vertical white lines indicate the time of odor valve opening. Color scale shows significant auROC values ($p < 0.01$, permutation test). Black boxes indicate bins with non-significant auROC values ($p > 0.01$, permutation test). Arrows indicate the same cell as that in (Figure 11). Lower panel: mean cell auROC values. Green line indicates go odor cue presentation versus baseline; pink dashed line indicates no-go odor cue presentation versus baseline. Shaded areas represent 95% confidence intervals. The vertical black dashed line indicates the time of odor valve opening. Note that across the population, mean auROC values did not differ significantly between go and no-go odor cue presentation at each time point ($p < 0.01$, Welch's t test).

(B) Neural response similarity measures between go and no-go odor cue presentation. Upper panel: examples of auROC values during the go/no-go odor cue presentation phase for one cell (same cell as in Figure 11) and the correlation coefficient of auROC values during the go/no-go-cue odor presentation phase. Lower panel: comparison of the correlation coefficients and cell-shuffled data, calculated for different pairs of cells. Neuronal response profiles were more similar between odor cues for paired responses from the same neuron (red) than for responses of two different neurons (black) ($p < 10^{-13}$, two-sample Kolmogorov–Smirnov test).

3.2. Behavior-specific activity of vTT cells in the odor-guided go/no-go task

Many vTT cells exhibited an increase in firing rate during specific behaviors over the course of the odor-guided go/no-go task (Figure 5A). Time intervals between behavioral events (the time from odor valve opening until the mouse withdrew its snout from the odor port, and the time from odor port withdrawal until reward port entry) also varied across trials (colored shaded areas in Figure 5A). To develop an overall firing profile accounting for this variability, we created event-aligned spike histograms (EASHs) (Ito and Doya, 2015). An EASH was derived by linearly scaling time

intervals between behavioral events in each trial and the median interval for all trials (Figure 5B, see Materials and methods). The EASHs clearly demonstrated that individual vTT cells were activated during different behavioral epochs (between-event intervals), such as when mice were poking the odor port in the approach epoch (plots in bottom left, Figure 13A) and during the odor-sampling epoch (plots second from the bottom left, Figure 13A).

To quantify neural activity across behavioral epochs during the go trials, we calculated changes in event-aligned firing rates from baseline (pre-odor cue period, 1.2 to 1 sec before odor port entry) in sliding bins (width, 100 msec; step, 20 msec) using ROC analysis. Across the population, almost all vTT cells exhibited a significant increase in firing rates during a specific behavior in each epoch (right color map in Figure 13A). Furthermore, individual vTT cells exhibited a significant decrease in firing rates in certain epochs. These results were independent of the size of the window in which auROC values were calculated (Figure 14). To evaluate the relationships between epoch-specific firing rates, vTT cells were classified into five groups based on their tuning peak time (Figure 7, see Materials and methods) with reference to the five go trial behavioral epochs. For each cell group, we calculated relative distributions of significant responses (Figure 8, see Materials and methods) for each bin, according to significantly increased or decreased changes in firing rate throughout the tasks (Figure 13B). Of vTT cells, 7% exhibited tuning peak times within the time window of the approach epoch, indicating a significantly greater probability of exhibiting an increase in firing rate during the approach epoch; 24% had tuning peak times during the odor-sampling epoch, indicating that the firing rates of these cells were increased

during the odor-sampling epoch; 23% and 11% had tuning peak times during the moving and waiting epochs, respectively, indicating that these cells were tuned to each epoch; and 15% had tuning peak times during the drinking epoch, indicating that they were tuned to the drinking epoch. Moreover, we observed that these classified cells tended to decrease their activity during other behavioral epochs, suggesting that individual vTT cells exhibit distinct tuning profiles for specific goal-directed behaviors.

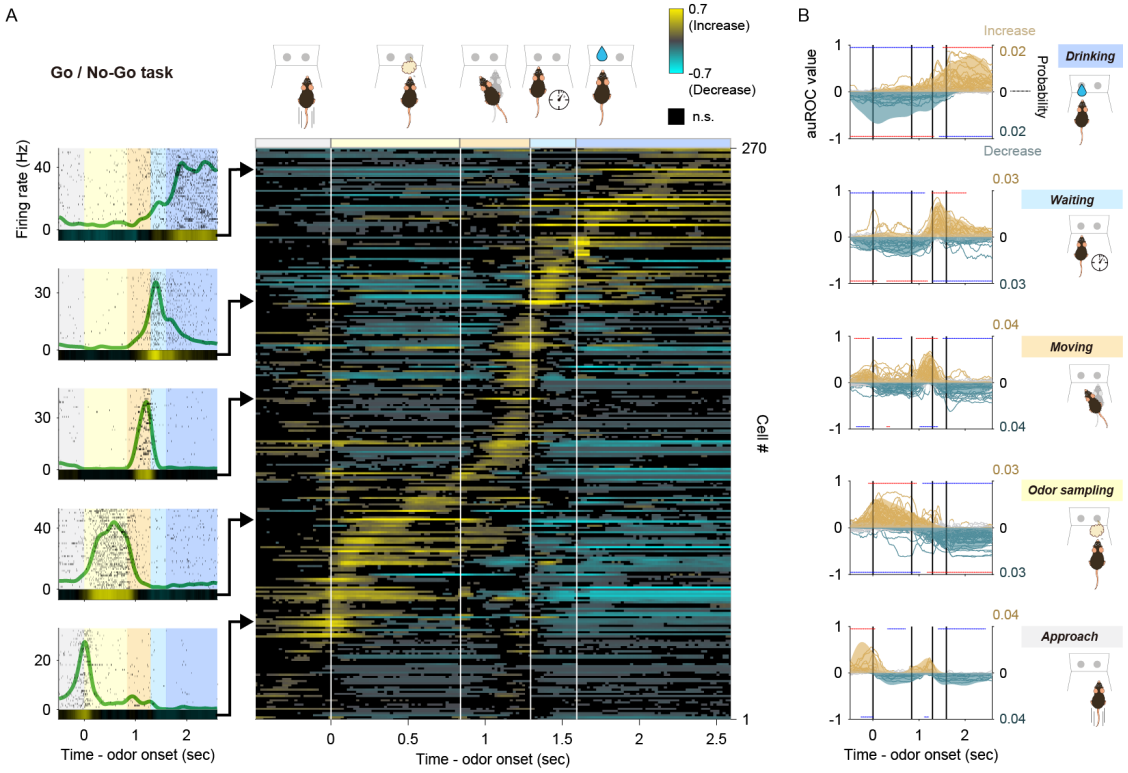

Figure 13 | Tuning of vTT cells to distinct behaviors in the odor-guided go/no-go task.

(A) Left panel: examples of event-aligned spike data for five representative cells tuned to specific behaviors. Event-aligned spike histograms were calculated using a 20 msec bin width and smoothed by convolving spike trains with a 60 msec wide Gaussian filter. Gray shading indicates the approach epoch (500 msec before odor port entry), yellow shading indicates the odor-sampling epoch (from entry into the odor port to exiting the odor port), orange shading indicates the moving epoch (from exiting the odor port to entry into

the water port), light blue shading indicates the waiting epoch (water reward delay, 300 msec before water valve was turned on), blue shading indicates the drinking epoch (1,000 msec after the water valve was turned on). Right panel: auROC values were calculated from event-aligned spike data (aligned by odor valve opening) for all cells, sorted by the peak time for auROC values. Each row corresponds to one cell. auROC values were calculated by comparing go correct trials to baseline (pre-odor cue period, 1.2 to 1 sec before odor port entry) in sliding bins (width, 100 msec; step, 20 msec). Vertical white lines indicate transitions between behavioral epochs, including odor port entry (corresponding to odor valve opening), odor port exit, water port entry, and water valve opening. The color scale for this figure is the same as that used in Figure 12A, with positive and negative values reflecting increased and decreased firing rates relative to baseline, respectively.

(B) Relative distribution of significant auROC values ($p < 0.01$, permutation test) per cell group tuned to a specific behavioral epoch in the odor-guided go/no-go task. Cell groups were tuned to the approach, odor-sampling, moving, waiting, and drinking epochs (from bottom to top graphs). Each line corresponds to one cell (left axes, auROC values). Yellow and blue indicate a significant increase and decrease from baseline, respectively. Gray indicates neither a significant increase nor decrease. Shaded regions show the relative distributions of significant auROC valves (right axes, probability, see Materials and methods). Red dots indicate that a time bin contained more cells with significant responses than in the distribution of 1,000 resampling datasets. Blue dots indicate that a time bin contained fewer cells with significant responses than in the distribution of 1,000 resampling datasets. Vertical black lines indicate the timing of odor port entry (corresponding to odor valve opening), odor port exit, water port entry, and water valve opening. Note that each cell group exhibited an excitatory response to a specific behavioral epoch, with suppressed responses relative to other epochs.

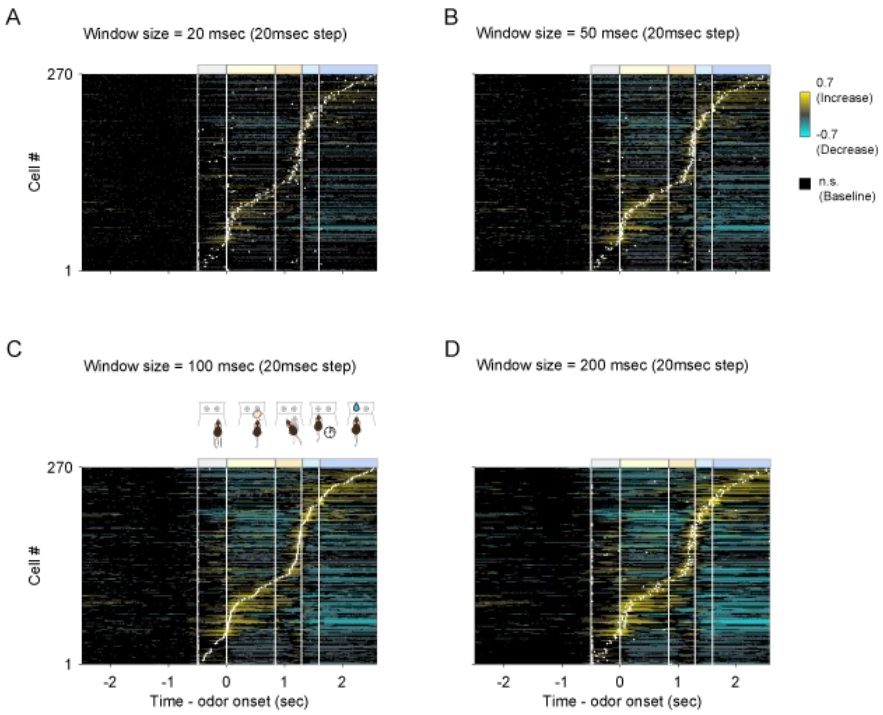

Figure 14 | Dependence of auROC values on window size in the odor-guided go/no-go task.

auROC values calculated during the odor-guided go/no-go task in window sizes of (A) 20 msec, (B) 50 msec, (C) 100 msec (as in Figure 13A), and (D) 200 msec. White dots indicate peaks of auROC values. Vertical white lines indicate transitions between behavioral epochs.

3.3. Behavior-specific activity of vTT cells in the odor-guided eating/no-eating task

3.3.1. Behavioral paradigms and indexes during the odor-guided eating/no-eating task

We observed that the activity of vTT cells was modulated across behavioral epochs on a hundreds-of-milliseconds timescale (Figure 13). We subsequently investigated how vTT cells would respond during each epoch if the behavioral epochs were prolonged to a multi-second timescale. Moreover, we also assessed whether the activity pattern of vTT cells in the go/no-go task could be generalized to different contexts and motivated behaviors. To this end, we performed an odor-guided eating/no-eating task with food rewards (Figure 15). Mice were placed on a food restriction schedule and trained to either choose to consume food in a dish or avoid consuming it

using dish odor-cuing. We randomly presented sugar on a dish with one of three different odor cues (eugenol, vanilla essence, or almond essence). The dish was then placed at an arbitrary position in the test cage. During the learning phase, eugenol and vanilla essence odors were associated with a sugar reward, whereas the almond essence odor was associated with a sugar reward followed by aversive consequences (a LiCl injection). After the learning phase, mice would approach the dish and proceed to consume its contents if either the eugenol or vanilla essence odor was presented (eating trials). Approximately 6 sec after the mouse began eating during the eating trials, the dish was removed even if the animal was still eating. The sequence of behaviors consistently exhibited by mice during the course of the eating trial epochs included approach (approaching the food dish), eating (from touching the dish to eating), and escape behaviors after food removal (Figure 15). In contrast, mice would approach the dish but not consume its contents if almond essence odor was presented (e.g., during no-eating trials) (Figure 15, No-eating). Powder (normal) chow was also presented on a dish in randomly interleaved trials. Behavior response accuracies for the cued odor trials and powder chow trials throughout all sessions were 0.93 ± 0.01, 0.90 ± 0.01, 0.96 ± 0.01, and 0.99 ± 0.003 (mean ± SEM, 63 sessions from six mice) for the eugenol, vanilla essence, almond essence, and powder chow trials, respectively.

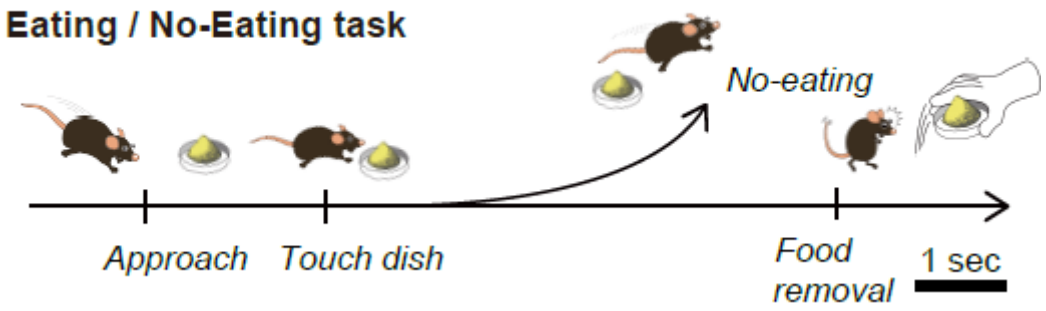

Figure 15 | Schematic of the odor-guided eating/no-eating task.

Behavioral epochs progressed temporally from left to right.

3.3.2. Tuning of vTT cells to distinct behaviors in the odor-guided eating/no-eating task

We recorded spike activity from 374 well-isolated vTT cells from six mice (Tables 3 and 4, recording positions are depicted in Figure 16) while mice performed the odor-guided eating/no-eating task. We observed that most vTT cells demonstrated an increase in firing rates during a specific behavior during the odor-guided eating trials. The graphs in Figure 17A (left side) show examples of behavior-specific vTT cells with greatly increased firing rates during each behavioral epoch. The duration of mouse behaviors during the task (approach, eating, and other behaviors such as locomotion, grooming, and freezing during dish removal) varied between trials (Figure 6A). We generated EASHs for the behavioral epochs of the odor-guided eating/no-eating task to develop an overall firing profile accounting for behavioral timing variability (Figure 6B). The EASHs clearly revealed that individual vTT cells were activated at different behavioral epochs, such as during the touching of the dish in the approach epoch (plots in bottom left, Figure 17A) and eating epoch (plots second from the bottom left, Figure 17A).

To quantify the neural activity modulated by behavioral epochs, we calculated the changes in event-aligned firing rates from baseline (pre-approach period, 3 to 1 sec before the onset of approach behavior) in sliding bins (width, 500 msec; step, 100 msec) using an ROC analysis approach. As shown in Figure 17A, most vTT cells exhibited an increase in firing in a specific behavioral epoch and a decrease in firing in the other two behavioral epochs. These results were independent of the size of the window in which auROC values were calculated (Figure 18). To evaluate these distinct patterns, we classified individual vTT cells into three types based on their tuning peak time with reference to the three different eating trial behavioral epochs. These analyses revealed that 19%, 20% and 12% of vTT cells had tuning peak times during the approach, eating and food removal epochs, respectively, suggesting that these three cell classes were tuned to specific and distinct behaviors.

To evaluate the firing pattern of these cellular subtypes during the eating trials, we calculated the relative distributions of significant responses for each bin according to significantly increased or decreased changes in firing rate throughout the tasks (Figure 17B). For each cell group, the occurrence probability in each bin with significantly increased firing rates during the most preferred epoch (i.e., the epoch in which vTT cells had a peak tuning time) was significantly higher than that of the cell-shuffled data. The occurrence probability of significantly decreased firing rate bins tended to emerge in the other epochs. These results suggest that vTT cells were tuned to specific odor-guided eating behaviors on a multi-second timescale.

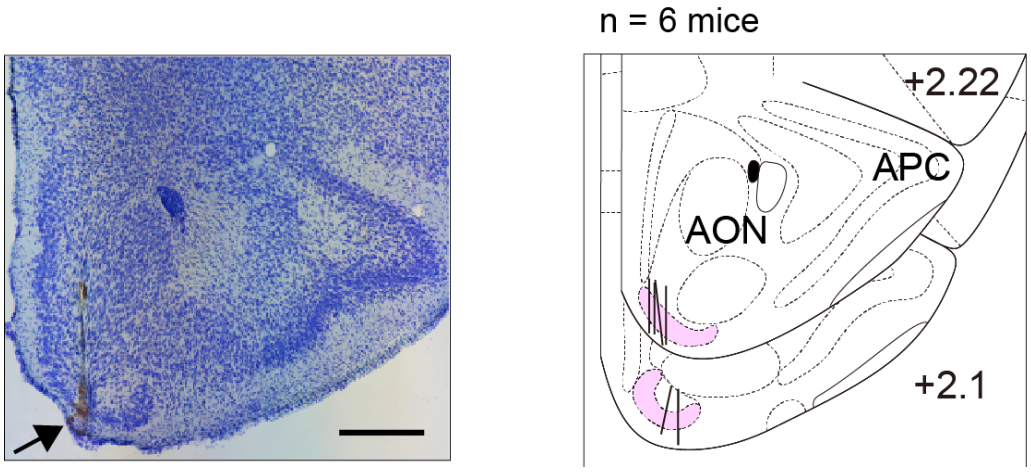

Figure 16 | The distribution of recording positions of the vTT in the odor-guided eating/no-eating task.

Nissl-stained frontal section (arrow indicates recording track) and recording tracks (vertical thick lines) of the vTT in the odor-guided eating/no-eating task. The pink area shows layer II of the vTT. APC, anterior piriform cortex; AON, anterior olfactory nucleus. Scale bar, 500 μm.

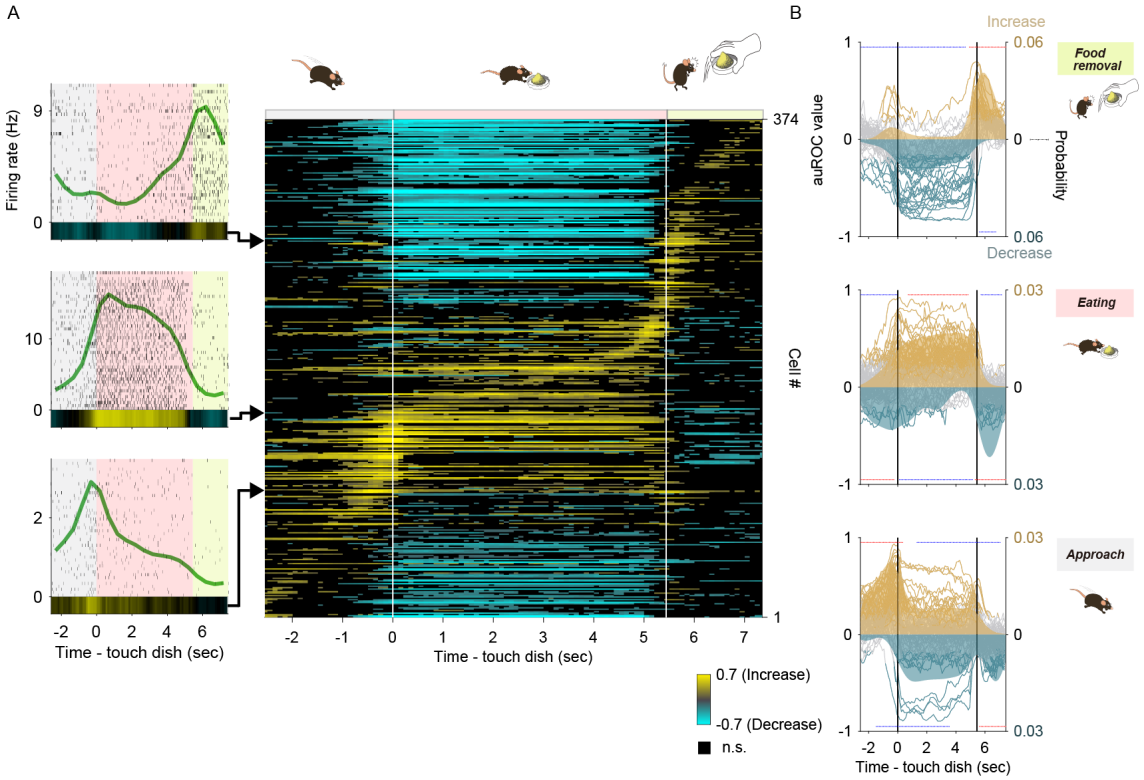

Figure 17 | Tuning of vTT cells to distinct behaviors in the odor-guided eating/no-eating task.

(A) Left panel: examples of event-aligned spike data for three representative cells tuned to specific behaviors. The event-aligned spike histograms were calculated using a 500 msec bin width and smoothed by convolving spike trains with a 500 msec wide Gaussian filter. Gray shading indicates the approach epoch (from the start

of approach behavior to contacting the dish), pink shading indicates the eating epoch (from the start of consumption to food removal), and light green shading indicates the food removal epoch (2 sec after food removal). Right panel: auROC values calculated from event-aligned spike data (aligned to contacting the dish) for all cells, sorted by the timing of the peak of auROC values. Each row corresponds to one cell. auROC values were calculated by comparing eating trials versus baseline (pre-approach period, 3 to 1 sec before starting approach behavior) in the sliding bins (width, 500 msec; step, 100 msec). Vertical white lines indicate when the animal touched the dish (left) and when the food was removed (right). The color scale indicates positive values that reflect increases in firing rate relative to baseline, while negative values reflect firing rate decreases relative to baseline.

(B) Relative distribution of the significant auROC values ($p < 0.01$, permutation test) in each cell group tuned to a specific behavior in the odor-guided eating/no-eating task. The cell groups were tuned to approach epoch, eating epoch, and food removal epoch (from bottom to top of graph). Each line corresponds to one cell (left axes, auROC values). Yellow and blue indicate a significant increase and decrease from baseline, respectively; gray indicates a non-significant increase or decrease. Shaded regions indicate the relative distribution of significant auROC valves (right axes, probability, see Materials and methods). Red dots indicate that a time bin contained more cells with significant responses than that in the distribution of 1,000 resampling datasets. Blue dots indicate that a time bin contained fewer cells with significant responses than that in the distribution of 1,000 resampling datasets. Vertical black lines indicate when mice contacted the dish (left) and when food was removed (right). Note that each cell group had an excitatory response to a specific behavioral epoch, with suppressed responses relative to other epochs.

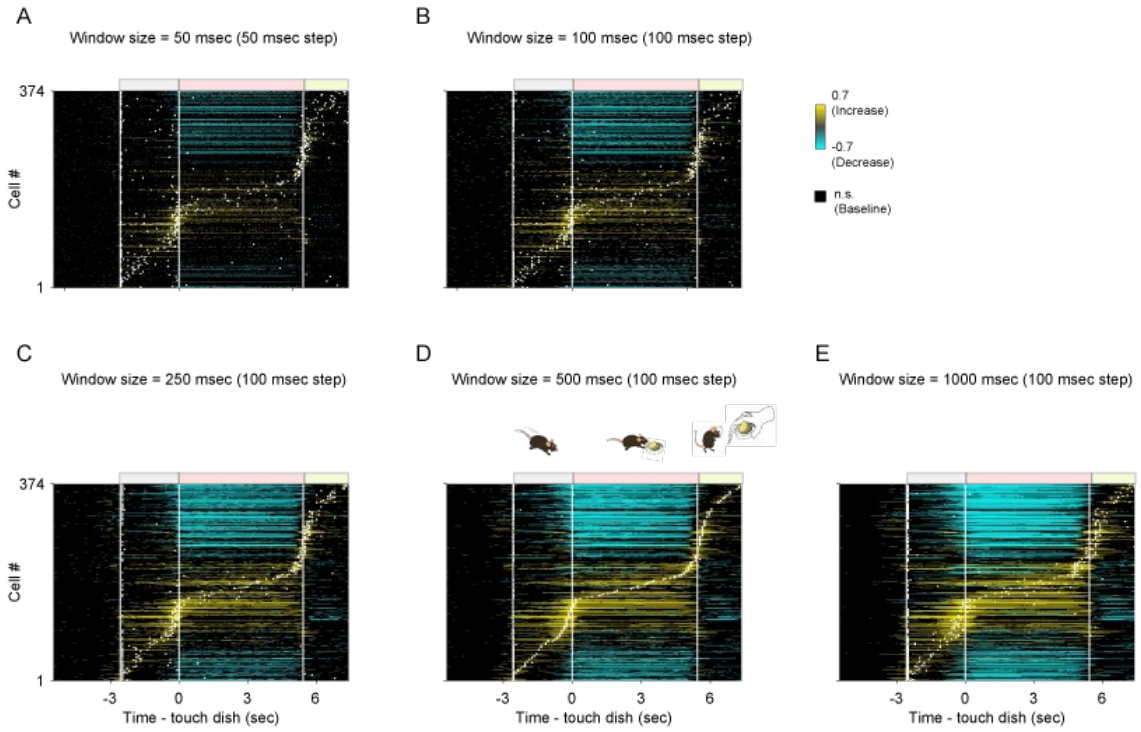

Figure 18 | Dependence of auROC values on window size in the odor-guided eating/no-eating task. auROC values calculated during the odor-guided eating/no-eating task in sliding bins of (A) width, 50 msec; step, 50 msec; (B) width, 100 msec; step, 100 msec; (C) width, 250 msec; step, 100 msec; (D) width, 500 msec; step, 100 msec (as in Figure 17A); and (E) width 1,000 msec; step, 100 msec. White dots indicate peaks of auROC values. Vertical white lines indicate transitions between behavioral epochs.

Table 3. Basic information in the odor-guided eating/no-eating task

Mouse	Recording sessions	Trials /session	Eating trials /session	No-Eating trials /session	Recorded cells /session
#1	6	48±2	36±2	12±0	6±2
#2	10	44±1	33±1	11±0	7±1
#3	6	55±2	44±2	11±0	6±1
#4	12	59±1	48±1	12±0	8±1

#5	10	55±2	45±2	11±0	5±1
#6	18	58±0	48±0	11±0	5±1

Table 4. The distribution of the vTT cell groups in the odor-guided eating/no-eating task

Mouse	Approach cells	Eating cells	Removal cells	Others	(Total)
#1	9	13	0	13	35
#2	31	20	1	17	69
#3	4	7	4	19	34
#4	7	24	9	51	91
#5	8	4	15	21	48
#6	12	8	16	61	97
(Total)	71	76	45	182	374

3.3.3. Odor responsivity among the eating trials in the odor-guided eating/no-eating task

To address whether the increased firing of cells during the eating epoch was driven by the odors associated with the food dish, we compared mean cellular auROC values of the eating epoch during eugenol, vanilla essence, and powder chow presentation across cells with tuning peak times during the eating epoch (Figure 19). A significant difference in firing rate increases between vanilla essence and powder chow presentations was observed. No significant difference was observed in

firing rate increases between eugenol and vanilla essence presentation or between eugenol and powder chow presentation, implying that vTT cells increase their firing during eating epoch behaviors in a manner largely independent of the type of odor cue.

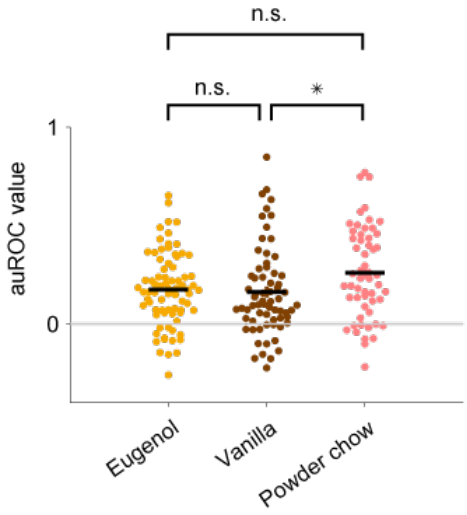

Figure 19 | Eating epoch activity during eugenol, vanilla essence, and powder chow presentation in the odor-guided eating/no-eating task.

Mean auROC values during the eating epoch for each cell which had a tuning peak time during the eating epoch (eugenol presentation, n = 76 cells; vanilla essence presentation, n = 67 cells; powder chow presentation, n = 55 cells). Only cells with a minimum number of 10 trials for each condition were included in these data. Statistical significance among three groups (*P < 0.05) was assessed using one-way analysis of variance (ANOVA).

3.4. Comparison of behavior-specific activity of vTT cells between different odor-guided tasks

3.4.1. Firing properties and the anatomical distributions of the classified cells

To further identify the common properties of vTT cell activity across distinct tasks, we first assessed the firing properties of vTT cells between tasks. No significant differences in baseline firing rates were observed between tasks (Figure 20A, p > 0.05, Wilcoxon rank-sum test). No

significant differences were noted in mean firing rates in the classified cell populations during each of the most preferred epochs (Figure 20B, $p > 0.05$, Tukey's test). Analysis of the anatomical distribution of the classified cells in both tasks revealed a varied distribution pattern within the vTT (Figure 21 and 22).

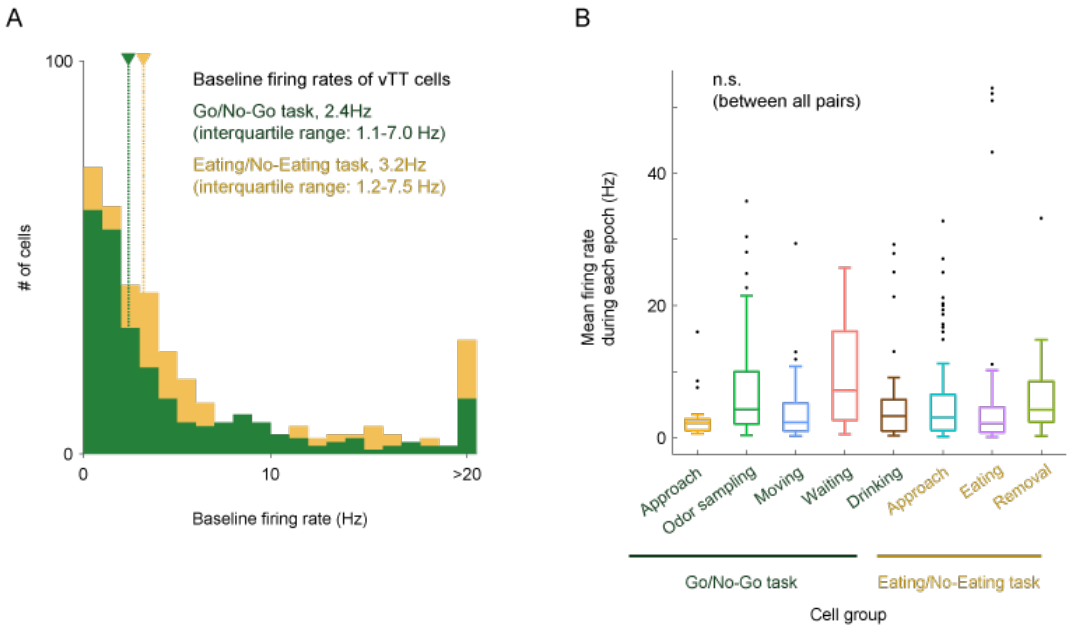

Figure 20 | Comparison of baseline and mean firing rates of each classified group between tasks.

(A) Distribution of baseline firing rates between tasks. The median baseline firing rates (for the odor-guided go/no-go task, pre-odor cue period, 1.2 to 1 sec before odor port entry; odor-guided eating/no-eating task, pre-approach period, 3 to 1 sec before the onset of approach behavior) were 2.4 Hz (interquartile range: 1.1-7.0 Hz) (green dashed line) in the go/no-go task (n = 270 cells), and 3.2 Hz (interquartile range: 1.2-7.5 Hz) (yellow dashed line) in the eating/no-eating task (n = 374 cells). Note that baseline firing rates were not significantly different between tasks ($p > 0.05$, Wilcoxon rank-sum test).

(B) Comparison of the mean firing rates across epochs. No significant differences in the mean firing rates of the classified cell populations between all-pairs were noted ($p > 0.05$, Tukey's test).

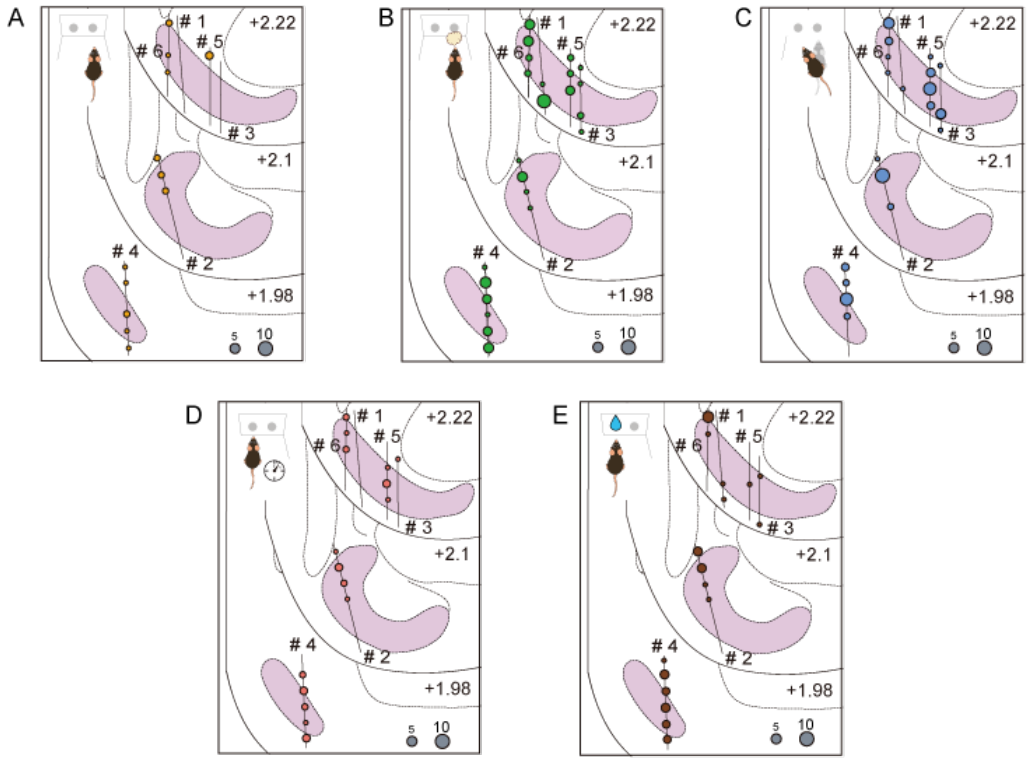

Figure 21 | Anatomical distribution of classified vTT cells in the odor-guided go/no-go task.

Each circle indicates the number of classified cells based on the position of tuning peak times. The cells were classified into (A) approach epoch, (B) odor-sampling epoch, (C) moving epoch, (D) waiting epoch, and (E) drinking epoch in the odor-guided go/no-go task. Each gray circle indicates the number of cells. Numbers correspond to individual mouse numbers in Table 2.

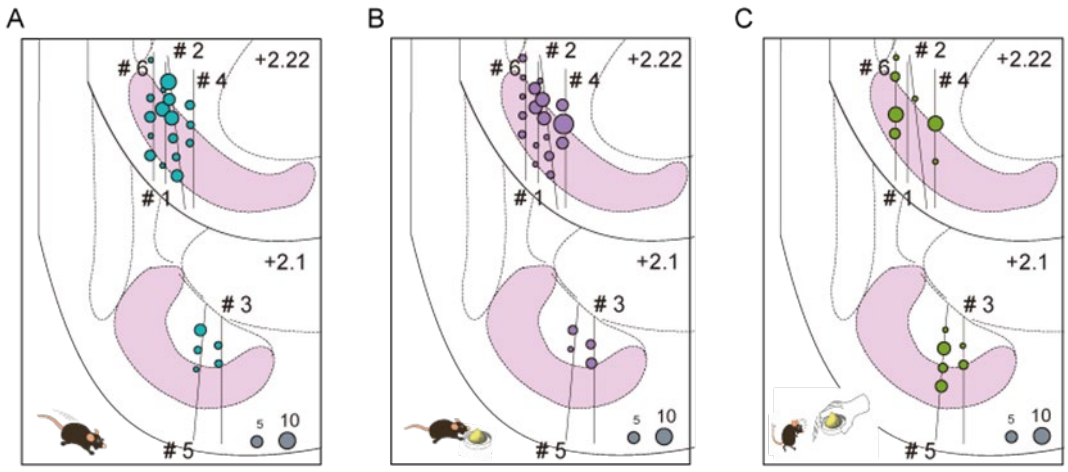

Figure 22 | Anatomical distribution of classified vTT cells in the odor-guided eating/no-eating task.

Each circle indicates the number of classified cells based on the position of tuning peak times. The cells were classified into (A) approach epoch, (B) eating epoch, and (C) removal epoch in the odor-guided

eating/no-eating task. Gray circles indicate the number of cells. The numbers correspond to individual mouse numbers in Table 4.

3.4.2. Correlation between the median of neural tuning durations and that of behavioral epoch durations

We then characterized and compared the firing time length and peak firing positions of vTT during the most preferred epoch. We investigated whether the tuning durations (Figure 7, see Materials and methods) of vTT cells corresponded to the actual durations of behavioral epochs. Three behavioral epochs (odor-sampling, moving, and waiting) were selected from the go/no-go task. The approach and eating epochs of the eating/no-eating task were also assessed based on the precisely defined start and end times of behavioral epochs within each trial. We then compared the distribution of tuning durations with behavioral durations in each epoch. The median for neural data was positively correlated with that of behavioral data ($r = 1.00$, $p < 10^{-3}$, Figure 23), suggesting that the duration of sustained discharge in vTT cells was dependent on the duration of the behavioral epoch.

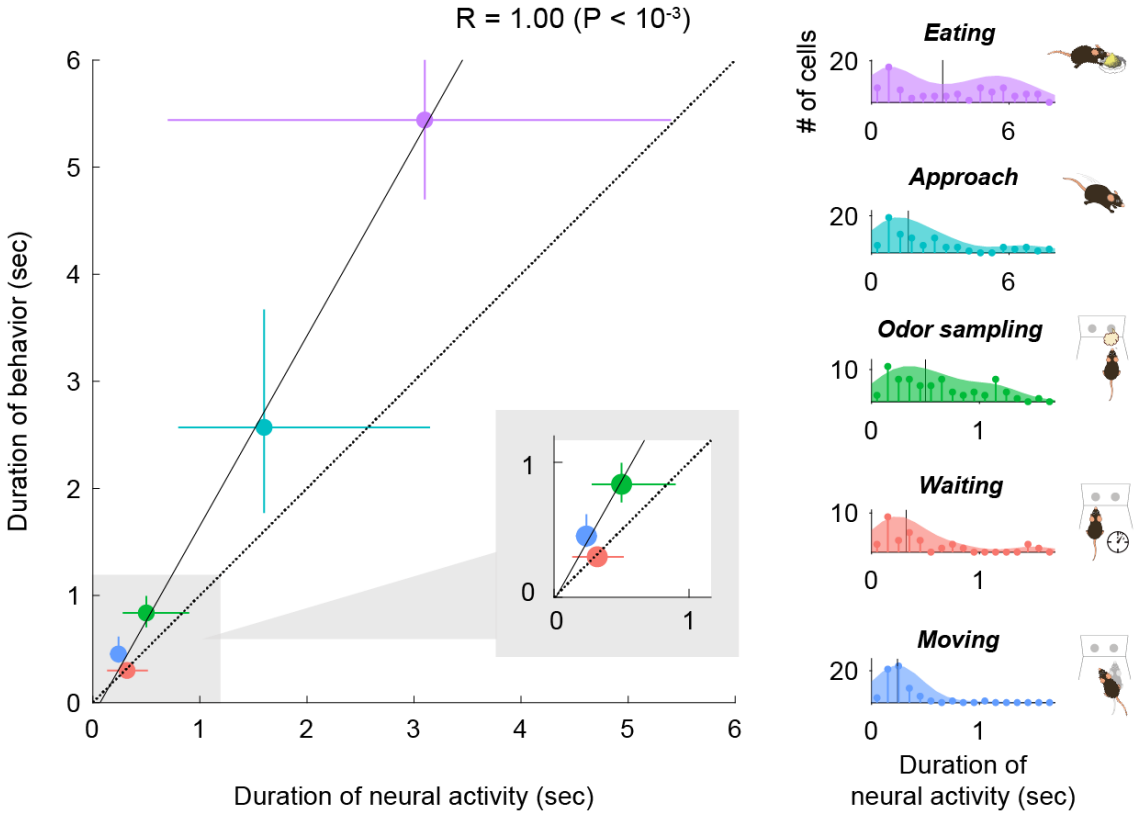

Figure 23 | Correlation between the median of neural tuning durations and that of behavioral epoch durations.

Right histograms show the distribution of neural tuning durations for each behavioral epoch (light blue, cell group tuned to approach epoch; purple, cell group tuned to eating epoch; green, odor sampling epoch; blue, moving epoch; red, waiting epoch). Vertical black lines in right graphs show the median tuning duration for each epoch. ($r = 1.00$, $p < 10^{-3}$ error bars show interquartile ranges).

3.4.3. Response profiles for tuning peak time and tuning duration across vTT cells with tuning peak times

We then examined the distribution of tuning peak times in relation to the time course of tasks. We aligned the tuning peak times of vTT cells as a function of task time course (Figure 24, top). We observed that the repertoire of vTT tuning peak times encompassed almost the entire continuing

series of behavioral epochs for odor-guided reward-directed behaviors. Thus, tuning durations overlapped with all task epochs.

We also observed that the distribution of tuning peak times tended to increase around transitions to the next behavioral epoch, such as when animals explored the odor and water ports during the go/no-go task, or arrived or departed from the dish in the eating/no-eating task (Figure 24, middle). Furthermore, a subset of the cells with tuning peak times around transitions between behavioral epochs tended to have shorter tuning duration (Figure 24, bottom), suggesting phasic activity around transitions. Indeed, during the eating epoch, the distribution of tuning durations exhibited a bimodal pattern (Figure 23 and 25). Most phasic responses tended to be located at the end of the eating epochs. Collectively, these results suggest that individual vTT cells were tuned to specific time windows (both tuning durations and tuning peak times) during goal-directed behaviors.

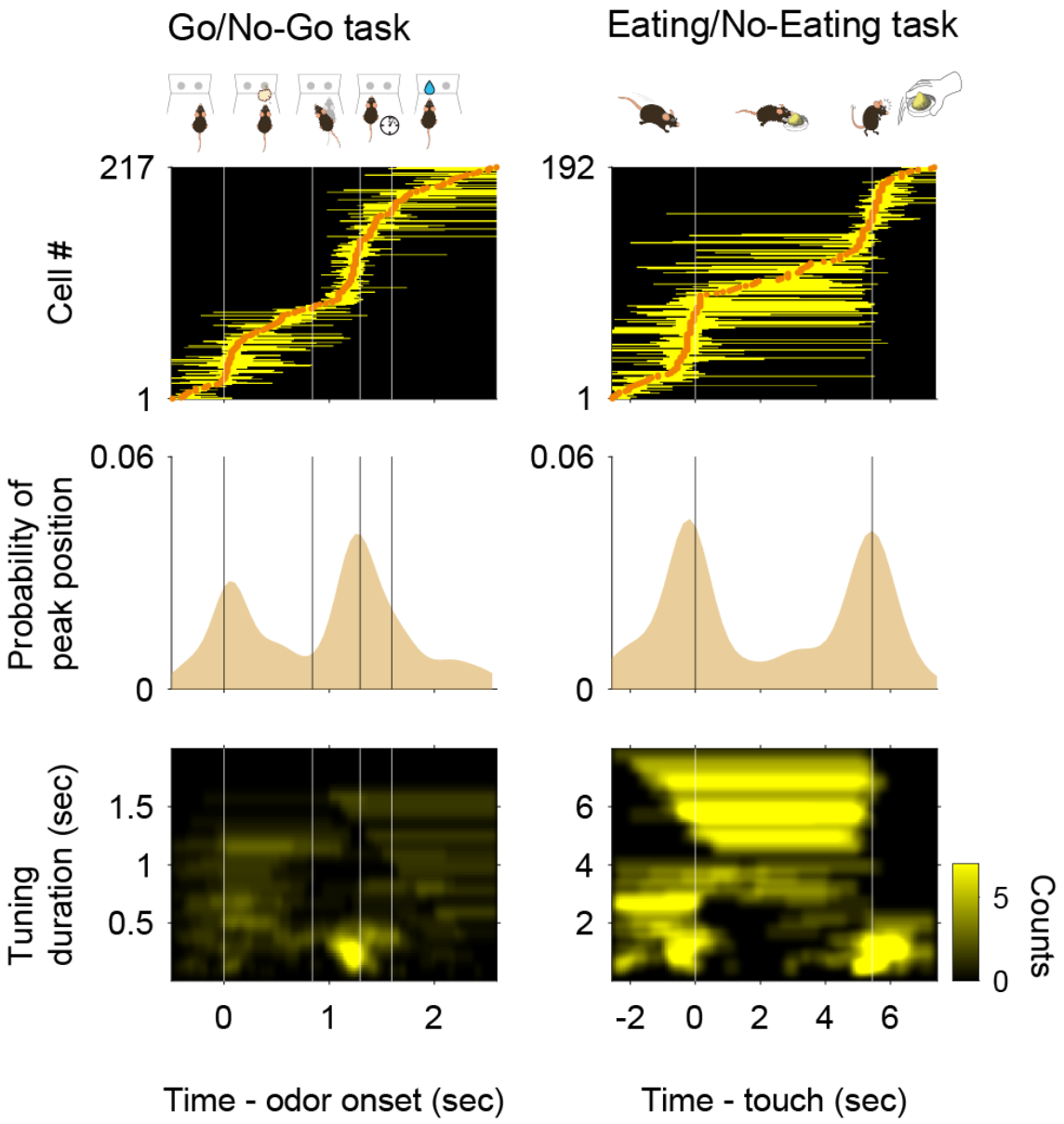

Figure 24 | Response profiles for tuning peak time and tuning duration across cells with tuning peak times.

Top panel: tuning peak times (orange dots) and tuning durations (yellow horizontal lines) in the odor-guided go/no-go task and odor-guided eating/no-eating task. Vertical white lines indicate transitions between the behavioral epochs. Center panel: distributions of tuning peak times along the task time course. Shades show tuning peak time distributions. Vertical black lines show transitions between the behavioral epochs. Bottom panel: distributions of excitatory tuning durations, which were defined as the duration of consecutive significant bins ($p < 0.01$, permutation test) with a 2-D Gaussian smoothing kernel. Vertical white lines indicate transitions between behavioral epochs. The color scale indicates the number of cells with each tuning duration in the tasks.

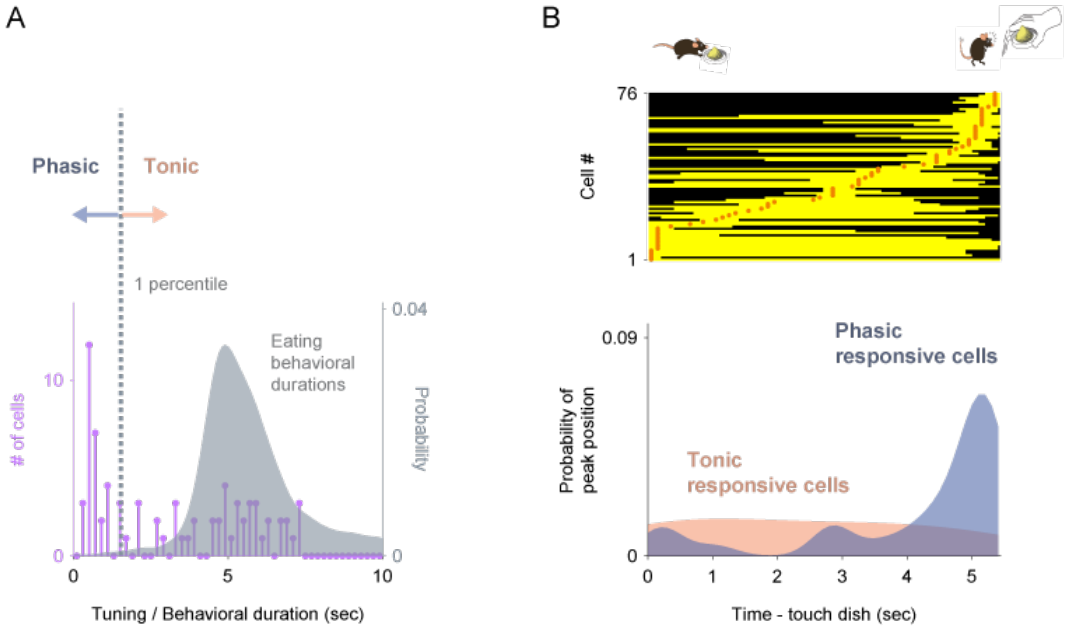

Figure 25 | vTT cells with tuning peak times in the eating epoch consisted of phasic and tonic responsive cells.

(A) We classified vTT cells with tuning peak times in the eating epoch (n = 76) into two types based on tuning duration. Cells with tuning durations shorter than one percentile of the eating duration (gray histogram) were defined as phasic responsive cells (n = 31); others were defined as tonic responsive cells (n = 45).

(B) There was a significant difference in the distributions of tuning peak times (orange dots) during eating behaviors between phasic and tonic responsive cells ($p < 10^{-4}$, two-sample Kolmogorov–Smirnov test). Note that the phasic responsive cells were mainly distributed before dish removal, and the tonic responsive cells tended to be uniformly distributed.

3.5. Behavioral context-dependent activity of vTT cells

3.5.1. Go-cue and no-go-cue preference around the odor sampling epoch in the odor-guided go/no-go task

We observed that many vTT cells tended to increase their firing rates before the most preferred behavioral epochs, and some cells maintained their increased firing rate after the epoch (Figures

13B, 17B, 24). We therefore hypothesized that individual vTT cell firing was tuned to a specific behavioral context and was thus dependent on specific task-elements during task progression rather than on specific behaviors. If this were true, the response patterns of vTT cells would change in a different context, even for the same behavior. We assessed nose poke behaviors during the odor-sampling epoch of the odor-guided go/no-go task and observed that a subset of cells exhibited differences in firing rates between the go and no-go trials just before the animals exited the odor port, despite involving the same nose-poking behavior. We quantified this by calculating go-cue versus no-go-cue trial preference using ROC analysis with real-time data. When the differences in firing rate were aligned to odor port exit times, we observed that more cells had differences in firing rate between the go and no-go trials before the animal exited from the odor port compared to that during the odor presentation phase (Figure 26). A subset of cells with tuning peak times not during the odor-sampling epoch also exhibited differences in firing rate just before odor port exit times.

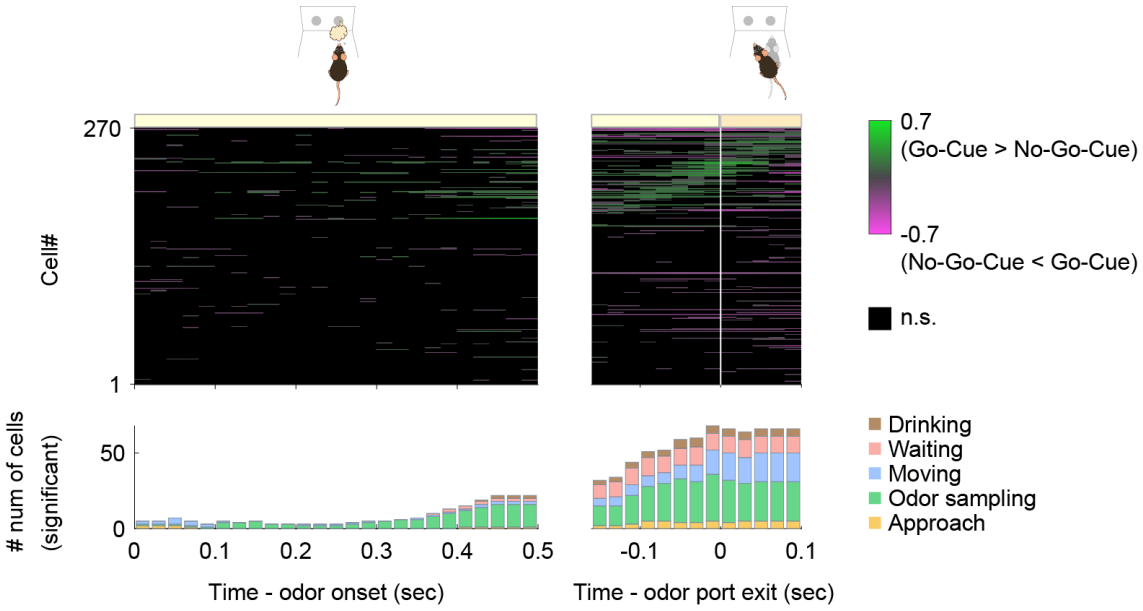

Figure 26 | auROC values for all cells around the odor sampling epoch in the odor-guided go/no-go task.

Upper panel: Each row corresponds to one cell. auROC values (left, aligned to the odor valve opening; right, aligned to the odor port exit) were calculated for correct go trials versus correct no-go trials in sliding bins (width, 100 msec; step, 20 msec). These values were sorted based on the time of peak auROC values in the right graph. The vertical white line indicates the time of odor port exit. The color scale indicates significant auROC values ($p < 0.01$, permutation test). The black boxes indicate bins with non-significant auROC values. Lower panel: the number of cells that exhibited significant auROC values ($p < 0.01$, permutation test) for each time bin (orange, cell group tuned to the approach epoch; green, odor sampling epoch; blue, moving epoch; red, waiting epoch; brown, drinking epoch).

3.5.2. The time course of odor decoding accuracy in the odor-guided go/no-go task

To examine whether the population activity of vTT cells could account for behavioral accuracy, we performed a decoding analysis to determine whether the firing rates of vTT cell populations could be used to classify each individual trial as go or no-go. We used support vector machines with linear kernels as a decoder (Cury and Uchida, 2010; Miura et al., 2012). Analyses of the decoding time course based on all 270 cells using a sliding time window revealed that decoding accuracy was maintained at chance levels during odor presentations and subsequently increased close to the level achieved during behavioral accuracy just before odor port exit (Figure 27). These results suggest that vTT cells were tuned to task elements in a particular behavioral context during goal-directed behaviors.

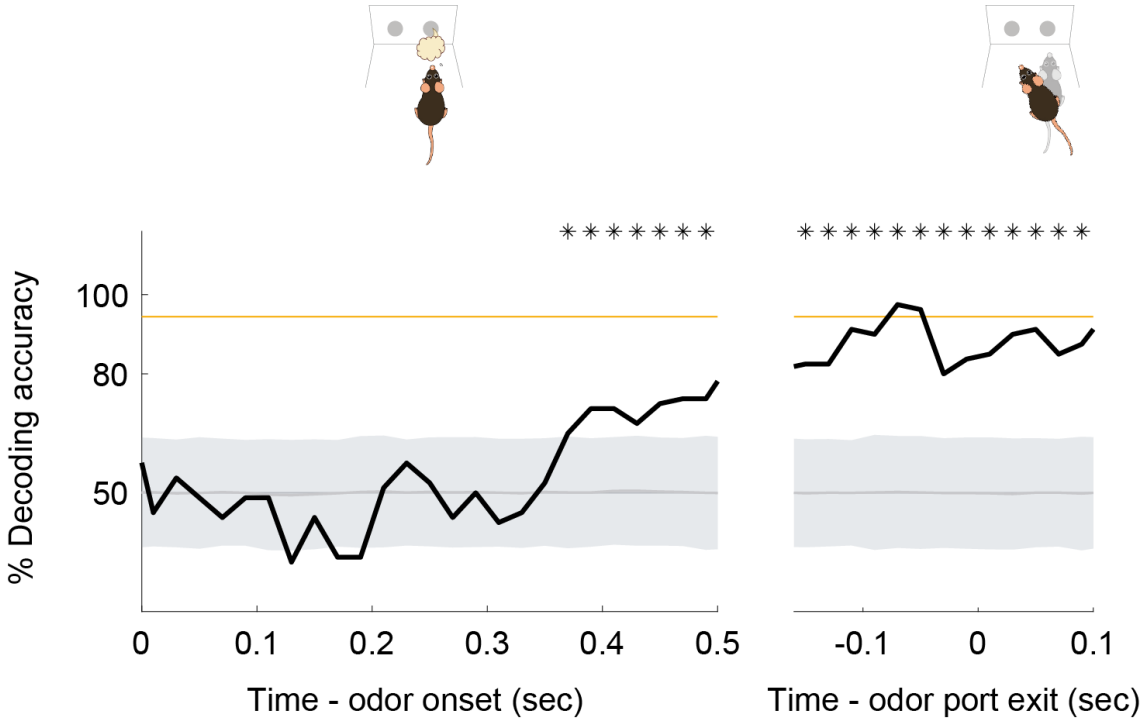

Figure 27 | The time course of odor decoding accuracy in the odor-guided go/no-go task.

A vector consisting of instantaneous spike counts for 270 neurons in a sliding window (width, 100 msec; step, 20 msec) was used as input for the classifier. Training of the classifier and testing were performed at every time point. The orange line indicates the level of behavioral performance. The gray line and shaded area indicate the mean ± 2SD of control decoding accuracies calculated from 1,000 trial-label-shuffled datasets. Top asterisks indicate accuracies greater than the mean + 2SD.

3.6. Cell types and connectivity patterns of vTT cells

3.6.1. Cell types of vTT cells

Although the majority of neurons in layer II of the vTT comprise pyramidal cells, the vTT also contains additional cell types (Haberly and Price, 1978; Neville and Haberly, 2004). To examine the distribution of glutamatergic and GABAergic cells in the vTT, we performed *in situ* hybridization to measure vesicular glutamate transporter 1 (VGluT1) and glutamic acid decarboxylase (GAD) 67 and GAD65 mRNA (*Slc17a7* and *Gad1/2* mRNAs, respectively) in the vTT (Figure 28).

Approximately 86% and 8% of vTT cells were *Slc17a7*-positive and *Gad1/2*-positive, respectively, suggesting that the principal neurons of the vTT are glutamatergic.

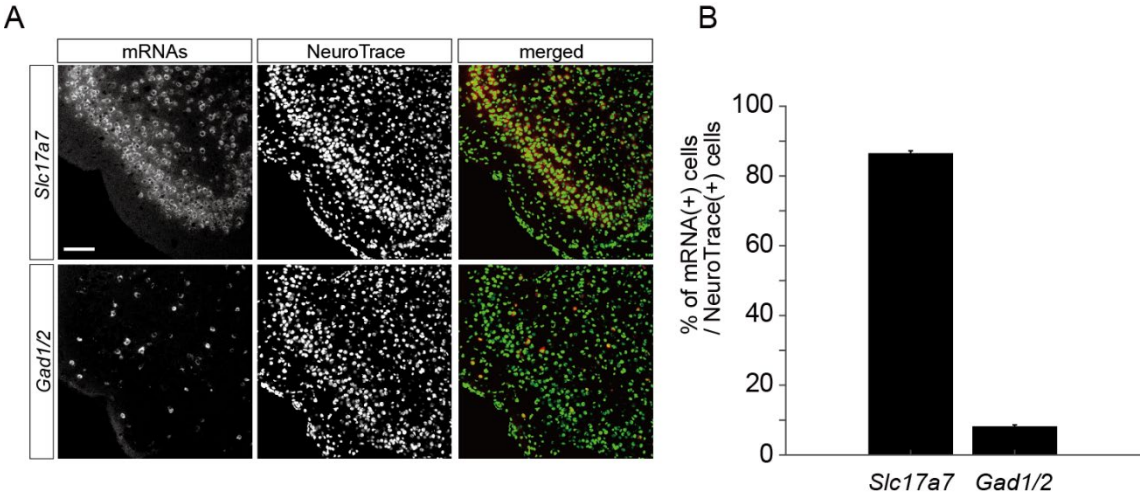

Figure 28 | Cell types of vTT cells.

(A) *In situ* hybridization of *Slc17a7* (upper panels) and *Gad1/2* (lower panels) mRNAs with Neurotrace staining of vTT cells. Scale bar, 100 μm.

(B) Average percentages of *Slc17a7*-positive cells (left column) and *Gad1/2*-positive cells (right column) among Neurotrace-positive cells in the vTT (n = 3 mice). Error bars indicate SEM.

3.6.2. Connectivity pattern of vTT cells

It has previously been reported that the vTT has reciprocal connections with the olfactory bulb (OB), anterior piriform cortex (APC), and posterior piriform cortex (PPC) (Igarashi et al., 2012; Luskin and Price, 1983a; Luskin and Price, 1983b). In addition, the deep layers of the vTT receive top-down inputs from the medial prefrontal cortex (mPFC) (Hoover and Vertes, 2011). To further examine cortical areas projecting to the vTT, we injected a retrograde tracer, cholera toxin B subunit (CTB) conjugated with Alexa 555, into the mouse vTT (Figure 29A). A number of retrogradely labelled (CTB-positive) cell bodies were identified in the OB, APC, PPC, and mPFC.

In contrast, CTB-positive cell bodies were rarely observed in the anterior olfactory nucleus (AON), which is located just dorsal to the vTT (Figure 29B).

To examine cortical regions that received axonal projections from vTT cells, we injected CTB into the mPFC, OB, AON, olfactory tubercle (OT), APC, and PPC. We then quantified retrogradely labelled CTB-positive cells in the vTT (Figure 29C, D). Many retrogradely labeled vTT cells were observed in mice that received CTB injections in the OB, AON, and APC. In contrast, only a small number of retrogradely labeled vTT cells were observed in mice that received CTB injections in the OT and PPC. Furthermore, retrogradely labeled cells were scarce in the vTT following injections of CTB into the mPFC. These results suggest that, in addition to dense reciprocal connections with the OB, the vTT projects to the AON and APC, and receives top-down projections from the APC, PPC, and mPFC (Figure 30).

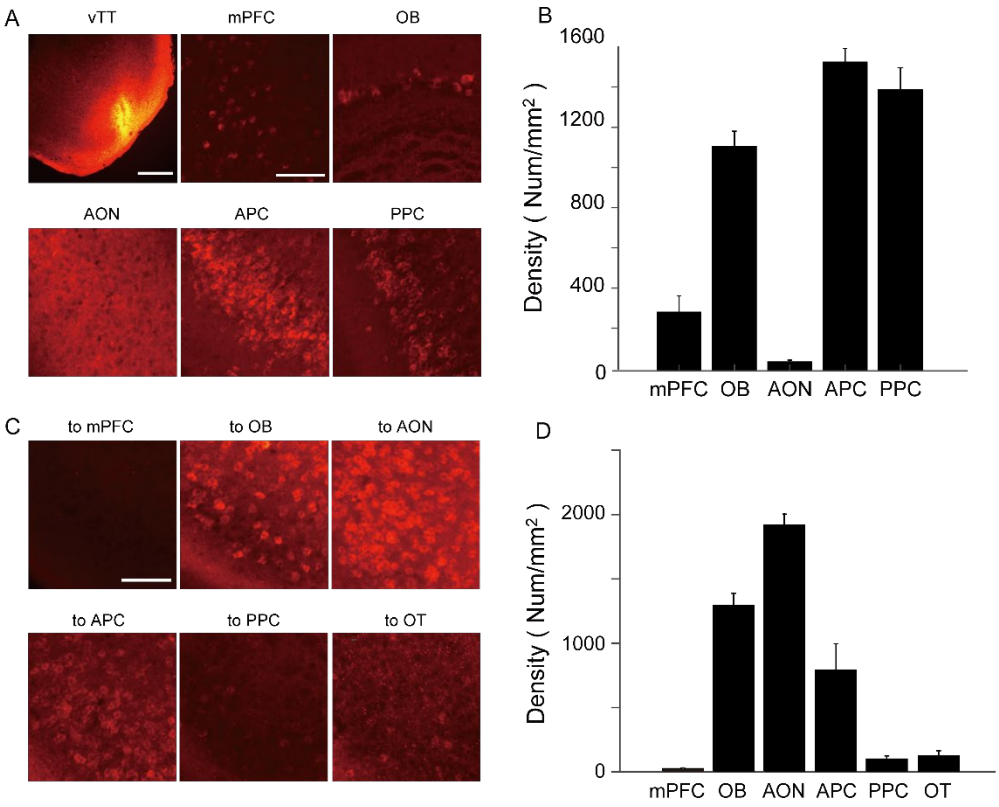

Figure 29 | Connectivity patterns of vTT cells.

(A) Upper left: Coronal section of the vTT after injection of Alexa 555-conjugated cholera toxin subunit B (CTB, red). Scale bar, 500 µm. The five other panels show CTB-labelled cells after CTB injections in the vTT. mPFC, medial prefrontal cortex; OB, olfactory bulb; AON, anterior olfactory nucleus; APC, anterior piriform cortex; PPC, posterior piriform cortex. Scale bar, 100 µm.

(B) Average density of CTB-labelled cell bodies in each area (mPFC, n= 5 from 3 mice; OB, n = 5 from 3 mice; AON, n = 3 from 2 mice; APC, n = 5 from 3 mice; PPC, n = 5 from 3 mice). Error bars indicate SEM.

(C) CTB-labelled vTT cells after injection of CTB into the mPFC (upper left), OB (upper middle), AON (upper right), olfactory tubercle (OT, lower left), APC (lower middle), and PPC (lower right). Scale bar, 100 µm.

(D) Average density of retrogradely labeled CTB-positive cells in the vTT (n = 3 from 2 mice). Error bars indicate SEM.

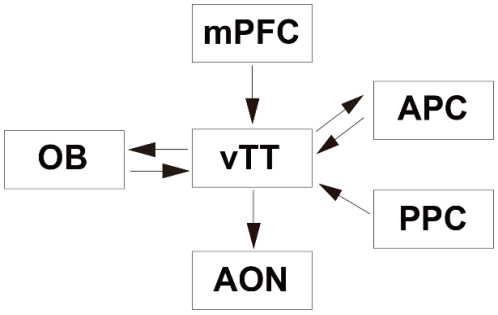

Figure 30 | Schematic diagram of vTT connectivity patterns. Arrows indicate axonal projections. mPFC, medial prefrontal cortex; OB, olfactory bulb; AON, anterior olfactory nucleus; APC, anterior piriform cortex; PPC, posterior piriform cortex.

Chapter 4. Discussion

4.1. The main findings of this study

The OC receives not only the afferent inputs from OB but also the efferent inputs from the higher brain regions. The vTT, the main target area in the present study, is an unexplored area of the OC and receives both bottom-up odor signals and top-down signals from higher brain areas. To the present, little is known about the roles of the vTT in odor-coding and integration of inputs. In this study, we reported the results of electrophysiological recordings of neuronal activity in the vTT in freely behaving mice during the performance of odor-guided behaviors. We characterized the neural activities of the vTT cells in mice performing two types of odor-guided goal-directed behavioral tasks. We found that individual vTT cells were highly tuned to a specific behavioral epoch of the learned tasks. Duration of the increased firings correlated with the time length of the behavioral epoch. The peak times of these increased firings in all recorded vTT cells covered nearly the entire time window for both tasks. The firing patterns of vTT cells showed contextual response changes despite the mice being in the same behavioral state. Furthermore, the vTT receives direct top-down inputs from mPFC and indirect inputs from other olfactory cortical area. Collectively, our results demonstrated characteristic tuning of individual vTT cells to specific temporal windows in the behavioral context of goal-directed tasks. These results also suggest that the context-dependent response of the vTT cells is represented by the top-down inputs from the mPFC and the vTT plays an important role in entraining specific information processing modes in olfactory areas by acting as

a hub that sends context-dependent signals to broad olfactory areas for adaptive odor-guided behaviors.

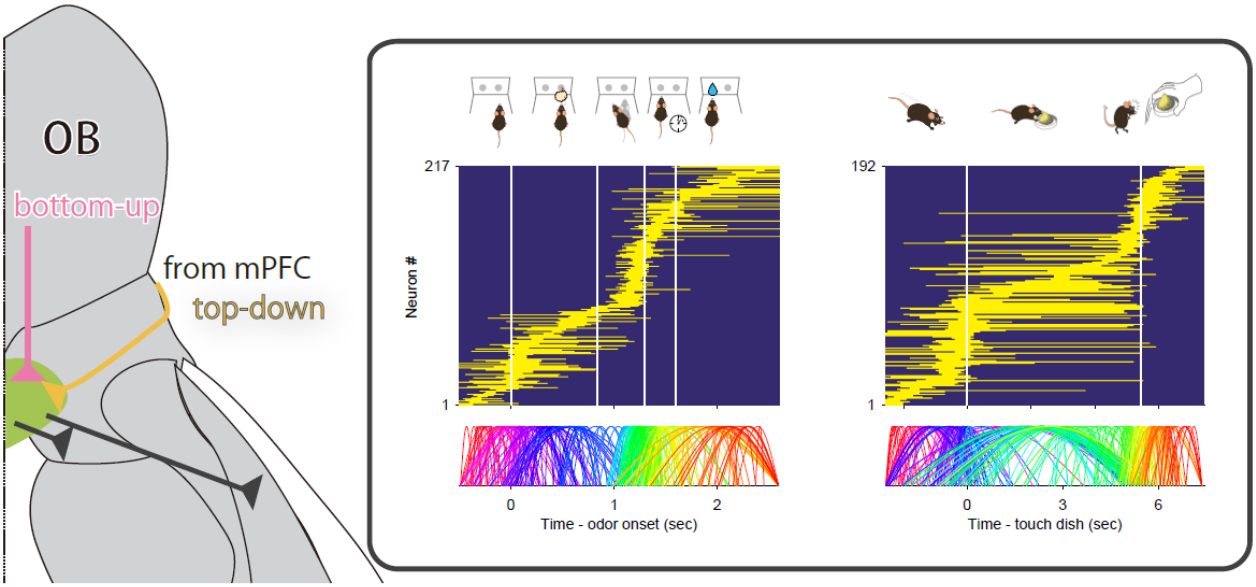

Figure 31 | A digest of the findings in the present study.

The left diagram shows the relashionship between the vTT and the other brain regions. The vTT receive the bottom-up inputs from the OB (pink) and also receive the top-down inputs from the mPFC (yellow). The right diagram shows that tuning vTT neurons to the distinct task elements of the goal-directed behaviors. Top panel: auROC values were calculated from event-aligned spike data (aligned by left: odor valve opening, right: touch the dish) for all cells, sorted by the peak time for auROC values. Each row corresponds to one cell. auROC values were calculated by comparing the trials (left: go correct trials and right: eating trials) to baseline in sliding bins, corresponding to each Figure (left: Figure 13 and right: Figure 17). Vertical white lines indicate transitions between behavioral epoch. The color scale with positive values reflecting increased firing rates relative to baseline (yellow). Bottom panel: Peaks and durations in individual cells are shown on a timescale (rainbow). The peak of the curve represents the position of the peak and the width of the curve represents the duration in individual vTT cells.

4.2. Activities of vTT cells in the odor representation phases

In the odor-guided go/no-go task, 25% of vTT cells exhibited increased firing during the learned odor presentation phases (Figures 11 and 12). Although many of these vTT cells exhibited peak firing ~100 msec after odor onset, they did not encode learned odor differences during the odor presentation phases (Figure 12B). Firing rate differences in a subset of cells emerged just before the odor port exit during which mice performed behavioral choices (Figures 26 and 27). These features resembled the response pattern for learned odor-guided tasks observed in the piriform cortex (PCx) (Gadziola et al., 2020; Gire et al., 2013). However, many vTT cells increased their firing rate before the odor presentation (Figures 12A, 13B, and 24), and individual vTT cells exhibited a particular tuning pattern characterized by peak tuning and tuning duration. Therefore, we hypothesized that the firing activity of vTT cells mainly reflected animal behavior and was dependent on task context.

4.3. Context-dependent neural activities in the vTT

4.3.1. Tuning of the vTT neurons to distinct task elements of goal-directed behaviors

During the odor-guided go/no-go task used here (Figure 13), vTT cells exhibited a specific firing rate tuning to each behavioral epoch (e.g., moving to the odor port, odor-sampling in the odor port, moving to the water reward port, waiting for the reward, and obtaining the water reward) of the go trials. Furthermore, these cells tended to suppress their firing activity during epochs other than the most preferred epoch.

To evaluate context-dependent tuning of vTT cells, we employed a different odor-guided task. We identified three unique cellular subtypes based on firing pattern differences that occurred

during the odor-guided eating/no-eating task (Figure 17). One cell type exhibited significant increases in firing during dish approach but tended to be silent during eating and food removal. A different subset of cells tended to fire more when the mouse approached the dish, during eating, and when the dish was removed. vTT cells also tended to suppress their firing during behavioral epochs other than their most preferred epoch.

Across tasks, we observed that tuning durations for each behavioral epoch correlated with the duration of behavioral epochs. In addition, the position of tuning peak times varied across the time course of the behavioral tasks (Figures 23 and 24). Further, many cells exhibited a short duration of activity at transitions between epochs, suggestive of a role in linking the two epochs (Figure 24). Moreover, we observed that vTT cells tuned to the odor-sampling epoch exhibited different activity between go and no-go trials just before odor port withdrawal (Figures 26 and 27), implying that individual vTT cells were tuned to a specific time window in task-modulated behavioral contexts rather than to a specific behavior.

Collectively, these results indicate that each vTT cell has a unique behavior- and context-dependent preference, demonstrated by tuning peak time and tuning duration. These properties of vTT cells may contribute to the representation of a series of specific behavioral context information (i.e., an episode) during odor-guided behaviors in the vTT. As vTT cells send their axons to other olfactory cortex areas such as the anterior olfactory nucleus (AON) and PCx (Figure 29) (Luskin and Price, 1983a; Luskin and Price, 1983b), we speculate that the vTT may provide information to widespread olfactory areas regarding moment-to-moment changes in

behaviors within certain behavioral contexts. Indeed, context-dependent modulation of neural activity is observed in mitral cells in the OB, an area that receives direct inputs from the vTT during the performance of odor-reinforcer association learning (Kay and Laurent, 1999).

4.3.2. The function of the vTT and its relationship to other olfactory cortical areas

We conjecture that behavioral context-dependent inputs from other higher-brain areas may contribute to the context-dependent activity of vTT cells because it is difficult to explain how behavioral context-dependent activity may otherwise be induced by bottom-up olfactory sensory input alone. The vTT receives direct top-down inputs from the mPFC and indirect inputs from other olfactory cortical areas (Luskin and Price, 1983b) (Figure 29). In particular, mPFC neurons are implicated in contextual encoding when animals move between different environmental contexts (Hyman et al., 2012) and preferentially fire at a specific position in the trajectory of a maze during a working memory task involving odor place-matching (Fujisawa et al., 2008). Along with the evidence presented here, these findings suggest that context-specific activity of the mPFC may contribute to the generation of context-dependent activity in the vTT. In addition, Allen et al. recently reported that odor cue-induced reward-predicting responses were not restricted to the olfactory cortex but occurred throughout the brain, including sensory, motor, and prefrontal cortices, as well as subcortical regions (Allen et al., 2019). Several studies have reported that not only the olfactory system, but also other sensory systems show context-dependent changes in their functional properties. The primary visual cortex (V1) neurons are accompanied by changes in their

functional properties in perceptual learning (Crist et al., 2001; Li et al., 2004). This functional change may be accompanied by changes in contextual influences in trained animals. The primary auditory cortex (A1) neurons recorded from ferrets trained to perform different auditory tasks (pitch detection or frequency discrimination) responded differently to the same auditory stimuli, depending on the behavioral contexts (Fritz et al., 2005). These findings suggest that context-dependent cells are located throughout the brain, and their activity may drive specific information processing modes in the brain. In this regard, the vTT may play an important role in entraining specific information processing modes in olfactory areas by acting as a hub, amplifier, or rectifier that sends context-dependent signals from the mPFC to broad olfactory areas. Neurons in the OT, part of the OC, encode goal-directed behavior and exhibit enhanced odor responses when animals selectively attend to specific odors (Carlson et al., 2018; Gadziola and Wesson, 2016). It is possible that the response characteristics of the OT reflect information processing modes from the vTT, and select the odor information necessary for the mode leading to appropriate behavior.

Based on the firing patterns in the task behavioral epochs, we classified vTT cells into five and three cell types for the odor-guided go/no-go task and odor-guided eating/no-eating task, respectively. The tuning durations of these cells were strongly correlated with behavioral epoch durations (Figure 23). However, the tuning durations of cells classified in the eating epoch showed a bimodal distribution, whereby some cells exhibited tuning durations that lasted for almost the entire eating epoch, and other cells exhibited short duration phasic responses. In addition, the neural activity of vTT cells was not always confined to a particular epoch. For example, many cells that

increased their firing rates during the eating epoch started to fire prior to this epoch (Figures 17 and 25). Moreover, individual vTT cells exhibited a unique tuning duration and tuning peak time (Figure 25). We speculate that a subset of vTT cells are tuned to smaller scale behaviors or task elements involving moment-to-moment changes in a particular behavioral context. For instance, vTT cells, which exhibited peak firing at the transition between epochs, especially in the eating/no-eating task, may encode the initiation of movement.

4.4. Putative encoding of internal states by vTT cells

During odor-guided goal-directed tasks, many vTT cells increased their firing rates prior to the onset of the most preferred behavioral epochs (Figures 13,17,23,24,26, and 27). These observations corroborate the idea that vTT cell activity is modulated both by signals during ongoing behavior as well as predictions about future behavior. Although a population of vTT cells increased their discharge rate during odor presentation in the odor-guided go/no-go task, their mean firing rate was not significantly different between go and no-go trials. Indeed, firing rate differences emerged just before mice exited the odor port. We speculate that vTT cell activity during the prediction of future behaviors was not driven directly by olfactory sensory inputs during ongoing behavior; rather, it was induced, directly or indirectly, by the piriform cortex and top-down inputs from higher cognitive and motivational centers in the prefrontal cortex (including mPFC) and amygdala. These regions play key roles in odor identification, odor discrimination, motivation, reward prediction, and decision-making. vTT cells fired with different intensities according to distinct cue types during

the eating epoch of the odor-guided eating/no-eating task (Figure 19). These response profiles may be underpinned by changes in the palatability of the reward flavors presented, since mice were exposed to both olfactory and taste stimuli during eating. Based on these results, we speculate that the firing patterns of vTT cells are influenced by both external contexts as well as internal states.

4.5. Study limitations

Despite its strengths, the present study did not address whether or how top-down inputs influence vTT cells in particular behavioral contexts. Further, we did not elucidate how vTT cells integrate bottom-up and top-down inputs. We have not investigated whether the context-dependent responses of vTT cells are also showed in other modalities, nor how they affect other olfactory cortical areas. Further work involving selective inhibition of top-down inputs or olfactory sensory inputs is needed to dissect the functional roles of vTT cells in odor-guided consummatory behaviors. Additionally, we need to demonstrate whether the vTT cells show the similar response with the other sensory task and inhibition of the vTT cells influence other olfactory cortical areas.

References

Allen WE, Chen MZ, Pichamoorthy N, Tien RH, Pachitariu M, Luo L, Deisseroth K. 2019. Thirst regulates motivated behavior through modulation of brainwide neural population dynamics. Science (80-) 364:eaav3932. doi:10.1126/science.aav3932

Asada H, Kawamura Y, Maruyama K, Kume H, Ding RG, Kanbara N, Kuzume H, Sanbo M, Yagi T, Obata K. 1997. Cleft palate and decreased brain gamma-aminobutyric acid in mice lacking the 67-kDa isoform of glutamic acid decarboxylase. Proc Natl Acad Sci U S A 94:6496–6499.

Bolding KA, Nagappan S, Han BX, Wang F, Franks KM. 2020. Recurrent circuitry is required to stabilize piriform cortex odor representations across brain states. Elife 9:1–23. doi:10.7554/eLife.53125

Buck L, Axel R. 1991. A novel multigene family may encode odorant receptors: a molecular basis for odor recognition. Cell 65:175–187.

Buschman TJ, Miller EK. 2014. Goal-direction and top-down control. Philos Trans R Soc L B Biol Sci 369. doi:10.1098/rstb.2013.0471

Carlson KS, Gadziola MA, Dauster ES, Wesson DW. 2018. Selective Attention Controls Olfactory Decisions and the Neural Encoding of Odors. Curr Biol 28:2195-2205 e4. doi:10.1016/j.cub.2018.05.011

Cavarretta F, Burton SD, Igarashi KM, Shep GM, Hines ML, Migliore M. 2018. Parallel odor processing by mitral and middle tufted cells in the olfactory bulb 1–15. doi:10.1038/s41598-018-25740-x

Choi GB, Stettler DD, Kallman BR, Bhaskar ST, Fleischmann A, Axel R. 2011. Driving opposing behaviors with ensembles of piriform neurons. Cell 146:1004–1015. doi:10.1016/j.cell.2011.07.041

Crist RE, Li W, Gilbert CD. 2001. Learning to see: Experience and attention in primary visual cortex. Nat Neurosci 4:519–525. doi:10.1038/87470

Cury KM, Uchida N. 2010. Robust odor coding via inhalation-coupled transient activity in the mammalian olfactory bulb. Neuron 68:570–585. doi:10.1016/j.neuron.2010.09.040

Felsen G, Mainen ZF. 2008. Neural Substrates of Sensory-Guided Locomotor Decisions in the Rat Superior Colliculus. Neuron 60:137–148. doi:10.1016/j.neuron.2008.09.019

Friedman B, Price JL. 1984. Fiber systems in the olfactory bulb and cortex: A study in adult and developing rats, Using the Timm method with the light and electron microscope. J Comp Neurol 223:88–109. doi:10.1002/cne.902230108

Fritz JB, Elhilali M, Shamma SA. 2005. Differential dynamic plasticity of A1 receptive fields during multiple spectral tasks. J Neurosci 25:7623–7635. doi:10.1523/JNEUROSCI.1318-05.2005

Fujisawa S, Amarasingham A, Harrison MT, Buzsáki G. 2008. Behavior-dependent short-term assembly dynamics in the medial prefrontal cortex. Nat Neurosci 11:823–833. doi:10.1038/nn.2134

Gadziola MA, Stetzik LA, Wright KN, Milton AJ, Arakawa K, Del Mar Cortijo M, Wesson DW. 2020. A Neural System that Represents the Association of Odors with Rewarded Outcomes and Promotes Behavioral Engagement. Cell Rep 32:107919. doi:10.1016/j.celrep.2020.107919

Gadziola MA, Wesson DW. 2016. The Neural Representation of Goal-Directed Actions and Outcomes in the Ventral Striatum's Olfactory Tubercle. J Neurosci 36:548–560. doi:10.1523/jneurosci.3328-15.2016

Ghosh S, Larson SD, Hefzi H, Marnoy Z, Cutforth T, Dokka K, Baldwin KK. 2011. Sensory maps in the olfactory cortex defined by long-range viral tracing of single neurons. Nature 472:217–222. doi:10.1038/nature09945

Gilbert CD, Sigman M. 2007. Brain states: top-down influences in sensory processing. Neuron 54:677–696. doi:10.1016/j.neuron.2007.05.019

Gire DH, Whitesell JD, Doucette W, Restrepo D. 2013. Information for decision-making and stimulus identification is multiplexed in sensory cortex. Nat Neurosci 16:991–993. doi:10.1038/nn.3432

Go Y, Niimura Y. 2008. Similar numbers but different repertoires of olfactory receptor genes in humans and chimpanzees. Mol Biol Evol 25:1897–1907. doi:10.1093/molbev/msn135

Haberly LB, Price JL. 1978. Association and commissural fiber systems of the olfactory cortex of the rat. II. Systems originating in the olfactory peduncle. J Comp Neurol 181:781–807. doi:10.1002/cne.901810407

Herrmann A. 2010. The Chemistry and Biology of Volatiles, The Chemistry and Biology of Volatiles. John Wiley and Sons. doi:10.1002/9780470669532

Hoover WB, Vertes RP. 2011. Projections of the medial orbital and ventral orbital cortex in the rat. J Comp Neurol 519:3766–3801. doi:10.1002/cne.22733

Hyman JM, Ma L, Balaguer-Ballester E, Durstewitz D, Seamans JK. 2012. Contextual encoding by ensembles of medial prefrontal cortex neurons. Proc Natl Acad Sci U S A 109:5086–5091. doi:10.1073/pnas.1114415109

Igarashi KM, Ieki N, An M, Yamaguchi Y, Nagayama S, Kobayakawa K, Kobayakawa R, Tanifuji M, Sakano H, Chen WR, Mori K. 2012. Parallel mitral and tufted cell pathways route distinct odor information to different targets in the olfactory cortex. J Neurosci 32:7970–7985. doi:10.1523/jneurosci.0154-12.2012

Ito M, Doya K. 2015. Distinct neural representation in the dorsolateral, dorsomedial, and ventral parts of the striatum during fixed- and free-choice tasks. J Neurosci 35:3499–3514. doi:10.1523/JNEUROSCI.1962-14.2015

Kay LM, Laurent G. 1999. Odor- and context-dependent modulation of mitral cell activity in behaving rats. Nat Neurosci 2:1003–1009. doi:10.1038/14801

Lak A, Okun M, Moss MM, Gurnani H, Farrell K, Wells MJ, Reddy CB, Kepecs A, Harris KD, Carandini M. 2020. Dopaminergic and Prefrontal Basis of Learning from Sensory Confidence and Reward Value. Neuron 105:700-711.e6. doi:10.1016/j.neuron.2019.11.018

Li W, Piëch V, Gilbert CD. 2004. Perceptual learning and top-down influences in primary visual cortex. Nat Neurosci 7:651–657. doi:10.1038/nn1255

Luskin MB, Price JL. 1983a. The laminar distribution of intracortical fibers originating in the olfactory cortex of the rat. J Comp Neurol 216:292–302. doi:10.1002/cne.902160306

Luskin MB, Price JL. 1983b. The topographic organization of associational fibers of the olfactory system in the rat, including centrifugal fibers to the olfactory bulb. J Comp Neurol 216:264–291. doi:10.1002/cne.902160305

Makinae K, Kobayashi T, Kobayashi T, Shinkawa H, Sakagami H, Kondo H, Tashiro F, Miyazaki J, Obata K, Tamura S, Yanagawa Y. 2000. Structure of the mouse glutamate decarboxylase 65 gene and its promoter: preferential expression of its promoter in the GABAergic neurons of transgenic mice. J Neurochem 75:1429–1437.

Malnic B, Hirono J, Sato T, Buck LB. 1999. Combinatorial receptor codes for odors. Cell 96:713–723. doi:10.1016/S0092-8674(00)80581-4

Manabe H, Kusumoto-Yoshida I, Ota M, Mori K. 2011. Olfactory cortex generates synchronized top-down inputs to the olfactory bulb during slow-wave sleep. J Neurosci 31:8123–8133. doi:10.1523/JNEUROSCI.6578-10.2011

Menini A, Lagostena L, Boccaccio A. 2004. Olfaction: From Odorant Molecules to the Olfactory Cortex. Physiology 19:101–104. doi:10.1152/nips.1507.2003

Miura K, Mainen ZF, Uchida N. 2012. Odor representations in olfactory cortex: distributed rate coding and decorrelated population activity. Neuron 74:1087–1098. doi:10.1016/j.neuron.2012.04.021

Miyamichi K, Amat F, Moussavi F, Wang C, Wickersham I, Wall NR, Taniguchi H, Tasic B, Huang ZJ, He Z, Callaway EM, Horowitz MA, Luo L. 2011. Cortical representations of olfactory input by trans-synaptic tracing. Nature 472:191–199. doi:10.1038/nature09714

Mori K, Nagao H, Yoshihara Y. 1999. The olfactory bulb: Coding and processing of odor molecule information. Science (80-). doi:10.1126/science.286.5440.711

Mori K, Manabe H, Narikiyo K, Onisawa N. 2013. Olfactory consciousness and gamma oscillation couplings across the olfactory bulb, olfactory cortex, and orbitofrontal cortex. Front Psychol 4:743. doi:10.3389/fpsyg.2013.00743

Mori K, Sakano H. 2011. How is the olfactory map formed and interpreted in the mammalian brain? Annu Rev Neurosci 34:467–499. doi:10.1146/annurev-neuro-112210-112917

Murata K, Kanno M, Ieki N, Mori K, Yamaguchi M. 2015. Mapping of Learned Odor-Induced Motivated Behaviors in the Mouse Olfactory Tubercle. J Neurosci 35:10581–10599. doi:10.1523/jneurosci.0073-15.2015

Murata K, Kinoshita T, Fukazawa Y, Kobayashi Kenta, Kobayashi Kazuto, Miyamichi K, Okuno H, Bito H, Sakurai Y, Yamaguchi M, Mori K, Manabe H. 2019. GABAergic neurons in the olfactory cortex projecting to the lateral hypothalamus in mice. Sci Rep 9. doi:10.1038/s41598-019-43580-1

Nagayama S, Enerva A, Fletcher ML, Masurkar A V., Igarashi KM, Mori K, Chen WR. 2010. Differential axonal projection of mitral and tufted cells in the mouse main olfactory system. Front Neural Circuits 4. doi:10.3389/fncir.2010.00120

Neville KR, Haberly LB. 2004. Olfactory Cortex In: Shepherd GM, editor. The Synaptic Organization of the Brain. Oxford Univ. Press. pp. 415–454.

Niimura Y, Nei M. 2005. Comparative evolutionary analysis of olfactory receptor gene clusters between humans and mice. Gene 346:13–21. doi:10.1016/j.gene.2004.09.025

Olender T, Nativ N, Lancet D. 2013. HORDE: Comprehensive resource for olfactory receptor genomics. Methods Mol Biol 1003:23–38. doi:10.1007/978-1-62703-377-0_2

Ono K, Takebayashi H, Ikeda K, Furusho M, Nishizawa T, Watanabe K, Ikenaka K. 2008. Regional- and temporal-dependent changes in the differentiation of Olig2 progenitors in the forebrain, and the impact on astrocyte development in the dorsal pallium. Dev Biol 320:456–468. doi:10.1016/j.ydbio.2008.06.001

Paxinos G. 2004. The mouse brain in stereotaxic coordinates / George Paxinos, Keith Franklin. London: Academic.

Raineki C, Shionoya K, Sander K, Sullivan RM. 2009. Ontogeny of odor-LiCl vs. odor-shock learning: similar behaviors but divergent ages of functional amygdala emergence. Learn Mem 16:114–121. doi:10.1101/lm.977909

Roelfsema PR, de Lange FP. 2016. Early Visual Cortex as a Multiscale Cognitive Blackboard. Annu Rev Vis Sci 2:131–151. doi:10.1146/annurev-vision-111815-114443

Roland B, Deneux T, Franks KM, Bathellier B, Fleischmann A. 2017. Odor identity coding by distributed ensembles of neurons in the mouse olfactory cortex. Elife 6. doi:10.7554/eLife.26337

Royet JP, Distel H, Hudson R, Gervais R. 1998. A re-estimation of the number of glomeruli and mitral cells in the olfactory bulb of rabbit. Brain Res 788:35–42. doi:10.1016/S0006-8993(97)01504-7

Shepherd GM. 2004. The Synaptic Organization of the Brain, The Synaptic Organization of the Brain. Oxford University Press. doi:10.1093/acprof:oso/9780195159561.001.1

Shidara M, Richmond BJ. 2002. Anterior cingulate: Single neuronal signals related to degree of reward expectancy. Science (80-) 296:1709–1711. doi:10.1126/science.1069504

Sosulski DL, Lissitsyna Bloom M, Cutforth T, Axel R, Datta SR. 2011. Distinct representations of olfactory information in different cortical centres. Nature 472:213–219. doi:10.1038/nature09868

Stettler DD, Axel R. 2009. Representations of Odor in the Piriform Cortex. Neuron 63:854–864. doi:10.1016/j.neuron.2009.09.005

Touhara K, Vosshall LB. 2009. Sensing odorants and pheromones with chemosensory receptors. Annu Rev Physiol. doi:10.1146/annurev.physiol.010908.163209

Uchida N, Mainen ZF. 2003. Speed and accuracy of olfactory discrimination in the rat. Nat Neurosci 6:1224–1229. doi:10.1038/nn1142

Uchida N, Poo C, Haddad R. 2014. Coding and transformations in the olfactory system. Annu Rev Neurosci. doi:10.1146/annurev-neuro-071013-013941

Wilson DA, Sullivan RM. 2011. Cortical processing of odor objects. Neuron 72:506–519. doi:10.1016/j.neuron.2011.10.027

Zhang X, Yan W, Wang W, Fan H, Hou R, Chen Y, Chen Z, Ge C, Duan S, Compte A, Li CT. 2019. Active information maintenance in working memory by a sensory cortex. Elife 8. doi:10.7554/elife.43191